Development of a xenon polarizer for magnetometry in neutron electric dipole moment experiments

By

Troy Dawson

A Thesis submitted to the Faculty of Graduate Studies of
The University of Manitoba
in partial fulfillment of the requirements for the degree of

MASTER OF SCIENCE

Department of Physics and Astronomy
University of Manitoba
Winnipeg

Dedication

To Anne, Dad, Mom and Jim

for always believing in me and supporting my studies.

Acknowledgments

I would like to thank my advisors, Jeff Martin and Chris Bidinosti, for their help and support during graduate studies. I would also like to thank Michael Lang and David Ostapchuk for their conversation and assistance around the lab during the last two years.

Abstract

Next generation electric dipole moment experiments require precise knowledge of the local magnetic fields in the experimental volume. Hyperpolarized xenon-129 has been proposed as a comagnetometer gas to be used in the neutron electric dipole moment experiment planned for TRIUMF. A flow through xenon polarizer was constructed and tested, and the hyperpolarized Xe-129 produced was transported to and characterized using a new AFP-NMR spectrometer. The polarization measured in the external AFP-NMR spectrometer was $(12 \pm 4)\%$. The longitudinal spin relaxation time T_1 was found to be (77 ± 24) s in the experimental NMR volume, limited by leaks and field inhomogeneity. This represents good progress towards the eventual system for nEDM experiments where polarizations greater than 50% and T_1, T_2 relaxation times greater than 1000 s are expected.

Contents

List of Figures

List of Tables

Chapter 1

Introduction

The Standard Model is a theory of particle physics that describes the fundamental building blocks of matter and the forces that mediate their dynamics, the strong force, the weak force and the electromagnetic force. To date, all experimental evidence is strongly supportive of the Standard Model. However, it can not account for the observed matter-antimatter (baryon) asymmetry of the universe. It is believed that CP violation (the violation of invariance under the combined charge conjugation (C) and parity (P) operators) needs to be present at levels greater than currently predicted in the Standard Model. Theories including new sources of CP violation beyond the Standard Model drive experimental searches for CP violation. One such search is for non-zero electric dipole moments of particles. This thesis is about the construction and characterization of a xenon polarizer used to produce hyperpolarized xenon which can be used in an experiment searching for a non-zero neutron electric dipole moment.

1.1 Search for a Neutron Electric Dipole Moment

Electric dipole moments (EDMs) arise from a spatial separation of charge within a particle. The Standard Model predicts an EDM for the neutron $|d_n| = 10^{-31} - 10^{-32}$ e $\cdot$ cm, if due to CP violation within the Cabibbo-Kobayashi-Maskawa (CKM) quark mixing matrix. If a larger neutron EDM is found it could signify new physics beyond the Standard Model. Another source of CP violation within the Standard Model arises from the θ-term of the quantum chromodynamics (QCD)

Lagrangian. The θ-term is the lowest order operator in this Lagrangian (dimension four) and is defined as [1]

$$\mathcal{L}_{dim=4} = \frac{g_s^2}{32\pi^2}\overline{\theta}G\tilde{G}, \tag{1.1}$$

where g_s is the strong coupling constant, $\overline{\theta}$ is a dimensionless constant, G and $\tilde{G}$ are the gluon field and its dual respectively and the indices have been suppressed. Experimentally, $|\overline{\theta}| < 10^{-11}$ and is constrained by the present experimental limit of the neutron EDM. The reason for the unnatural smallness of the $\overline{\theta}$ parameter is unknown, suggesting a fine tuning problem. The unexplained smallness of $\overline{\theta}$ is called the "strong CP problem". The smallness of $\overline{\theta}$ has led to a postulate of higher symmetry which would force $\overline{\theta}$ to be exactly zero. This Peccei-Quinn symmetry in turn leads to a prediction of new particles known as axions. To date, axions have never been discovered [1].

The observation of a non-zero neutron EDM would also be strongly related to predominance of matter over anti-matter in our universe today [2]. A set of three conditions must have been met at some point in the early universe in order for the baryon asymmetry to exist. This set of conditions is known as the Sakharov criteria [3, 4, 5]:

1. Baryon number B conservation is violated, because the net baryon number of the universe must have changed over time.

2. C and CP-symmetry are violated so that B-violating processes don't make as many baryons as antibaryons.

3. A departure from thermal equilibrium because the average baryon number would be constant in equilibrium.

The presence of a baryon asymmetry of the universe remains an unsolved problem in physics. Theories of new physics have been developed to explain the asymmetry.

Electroweak baryogenesis is an example of a theory that seeks to explain the baryon asymmetry using electroweak theory and new physics at the TeV scale . In electroweak baryogenesis, a strong

first order phase transition is postulated which results in bubbles of broken electroweak phase (satisfying criteria 3). B-violating reactions can then occur on the bubble walls through the sphaleron process (satisfying criteria 1). CP-violating processes occur inside and outside of the bubble which prevents the wash-out of the baryon asymmetry (satisfying criteria 2). A problem with electroweak baryogenesis is that additional CP-violation beyond the Standard Model is required to generate the correct magnitude of baryon asymmetry in the universe [5, 6].

In order to deal with this problem, new sources of CP-violation have been proposed. Often these new sources are presented in the context of new CP-violation for heavier particles than exist in the Standard Model. An example of this kind of theory involves supersymmetry, where the superpartners are postulated to be heavier than their Standard Model counterparts and possess increased CP violation [1].

While these theories can successfully explain the baryon asymmetry of the universe, they must be experimentally verified or falsified. Searching for a non-zero neutron EDM remains one of the best experimental avenues to discover new sources of CP-violation, both within (θ-term) and beyond (e.g. supersymmetric electroweak baryogenesis) the Standard Model.

The combined operation of CPT leaves all Standard Model interactions unchanged, under the assumption of Lorentz symmetry [2]. A T-violating process can therefore be considered a CP-violating process.

The existence of non-zero EDMs would signify a violation of T symmetry. To see this, consider a particle of spin $\vec{S}$ placed in an electric $\vec{E}$ and magnetic $\vec{B}$ field. The Hamiltonian is

$$H = -\mu\vec{B}\cdot\frac{\vec{S}}{S} - d\vec{E}\cdot\frac{\vec{S}}{S}, \tag{1.2}$$

where μ is the magnetic moment and d is the electric dipole moment. Under time reversal, $T\left(\vec{B}\cdot\vec{S}\right) = \vec{B}\cdot\vec{S}$ and $T\left(\vec{E}\cdot\vec{S}\right) = -\vec{E}\cdot\vec{S}$. Therefore, a non-zero EDM will violate T (and CP) symmetry.

1.2 Using Ultra Cold Neutrons for an EDM Experiment

Ultra Cold Neutrons (UCN) are extremely low energy neutrons, with kinetic energies of less than 300 neV. At this energy, the neutrons reflect off material walls, allowing for them to be trapped in bottles for extended periods of time. This characteristic allows for unique experiments to be undertaken. An example of such an experiment is a neutron EDM experiment. UCN interact via strong interaction with the fermi potential of the material walls, keeping the neutrons trapped inside a bottle. The neutron storage time in the bottle is limited by free neutron decay. Free neutrons decay via the weak force and have a mean lifetime of $\tau_n = 881.5$ s. UCN also interact with gravitational and magnetic fields.

In general, a neutron EDM is measured by placing UCN in an electric and magnetic field and measuring the Larmor frequency which is the frequency with which the spin will tend to precess about the fields. For parallel fields,

$$h\omega_0^{\uparrow\uparrow} = |2\mu_n B_0 + 2d_n E|\,, \tag{1.3}$$

where h is the Planck constant, $\omega_0^{\uparrow\uparrow}$ is the measured Larmor frequency with parallel fields, μ_n is the magnetic moment of the neutron, B_0 is the magnetic field magnitude, d_n is the electric dipole moment of the neutron and E is the electric field magnitude. Similarly, for anti-parallel,

$$h\omega_0^{\uparrow\downarrow} = |2\mu_n B_0 - 2d_n E|\,, \tag{1.4}$$

where $\omega_0^{\uparrow\downarrow}$ is the measured Larmor frequency with anti-parallel fields. Upon changing electric field directions the Larmor frequency will change by:

$$h\omega_0^{\uparrow\uparrow} - h\omega_0^{\uparrow\downarrow} = 4d_n E. \tag{1.5}$$

Therefore, by switching the direction of the electric field and measuring the shift in Larmor frequency, the neutron EDM can be measured.

1.2.1 Setup and Experimental Technique for ILL UCN-EDM Experiment

The best experimental upper limit on the neutron EDM is $d_n < 2.9 \times 10^{-26}$ e $\cdot$ cm, where e is the magnitude of the electron charge. This was achieved at Institut Laue-Langevin (ILL) in Grenoble, France [8]. The precision of their result was limited by statistics, as the UCN density in the EDM cell (21 L) was 0.7 UCN/cm^3. The basis of their EDM experimental approach is briefly described which is similar to ours and based on a nuclear magnetic resonance (NMR) technique.

At ILL a rotor souce is used to downscatter cold neutrons producing UCN [25]. Correct spin state UCN pass through a magnetized foil. The resulting polarized UCN are transported into an experimental volume possessing uniform magnetic and electric fields oriented either parallel or anti-parallel to one another. Then the precession frequency ω_0 is measured.

The experimental setup used at ILL is described in Figure 1.1. In this experiment, the precession frequency of the UCN is measured using a technique known as the Ramsey separated oscillatory field magnetic resonance method [9, 10, 11]. The method is portrayed graphically in Figure 1.2. In this method, the UCN are initially stored in the n-EDM measurement volume with their spins aligned with the vertical magnetic field B_0. A horizontal uniform oscillating field with amplitude B_1 and frequency ω is applied to the UCN for a time τ, in order to deflect their spins into the horizontal plane. This type of RF pulse is known as a $\frac{\pi}{2}$-pulse. (See Chapter 3 for a description of nuclear magnetic resonance, specifically Section 3.1.4 for information about a $\frac{\pi}{2}$-pulse.)

The B_1 field is then switched off. The spins now are allowed to precess freely in the horizontal plane at the Larmor frequency $\omega_0 = \gamma B_0$ (the effect of the electric field has been ignored for now) for a time T. A second, coherent (same phase), $\frac{\pi}{2}$-pulse is applied, and the UCNs are drained from the cell.

Decay time depends on the frequency ω of the applied B_1 field. By varying the frequency, a characteristic set of oscillations shown in Figure 1.3 is obtained. The peaks represent out of phase spin flips. The spin therefore precessed around the B_0 field for a total rotation angle of $n\pi$, where n is an odd integer. A valley, conversely, represents an in phase spin flip with a total rotation angle

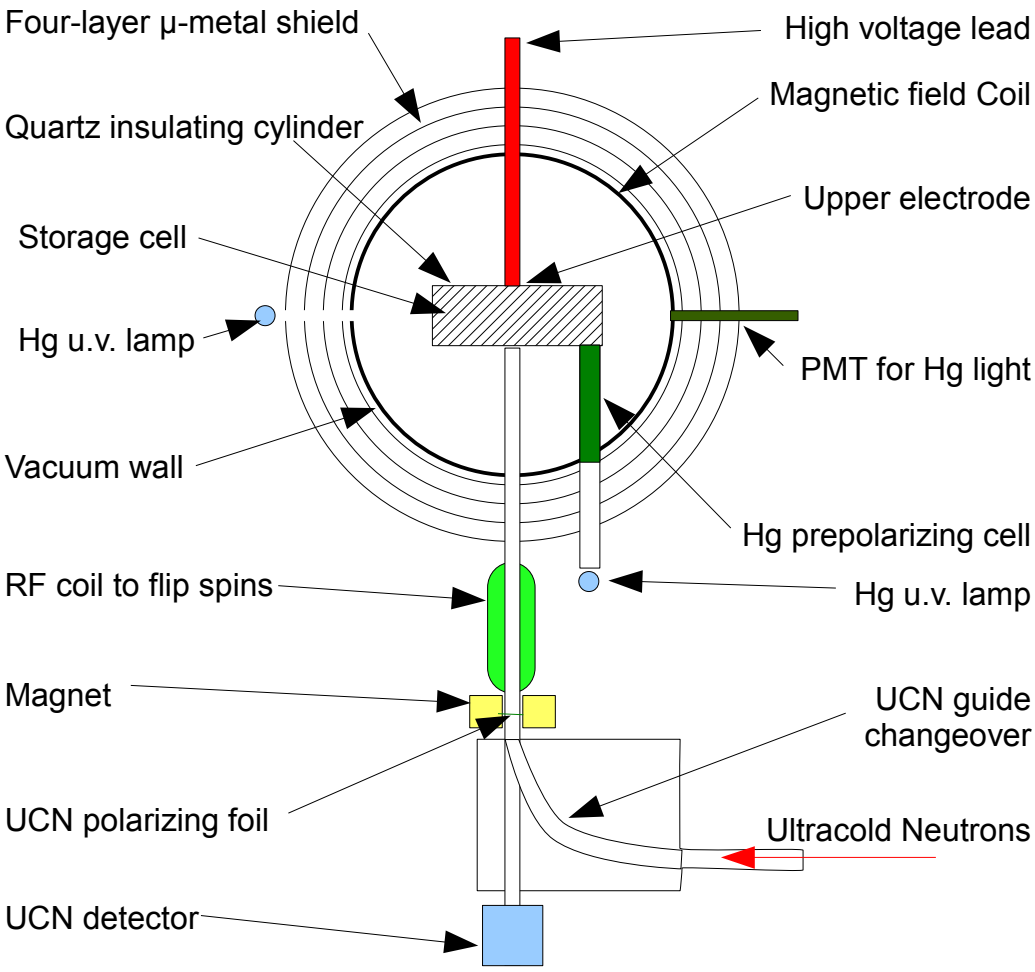

Figure 1.1: Experimental setup used for the present best experimental limit of the neutron EDM, at ILL [8]. UCN enter the apparatus at the bottom right. Only one spin state of UCN may pass through the polarizing foil and therefore the UCN transported to the storage cell are nearly fully polarized. The UCN are trapped in the storage cell by closing a door. The neutrons have remained aligned with the interior magnetic field (1 μT) through adiabatic spin transport. A DC electric field (12 kV/cm) is applied in a direction aligned with the magnetic field. RF pulses (B_1 field) are applied to measure the precession frequency as described in the text, using Ramsey's method. After the sequence, the door is opened and the neutrons leak out through the same polarizing foil, now used as a spin analyzer, and into a neutron detector. The Hg components are used for the Hg-199 comagnetometer.

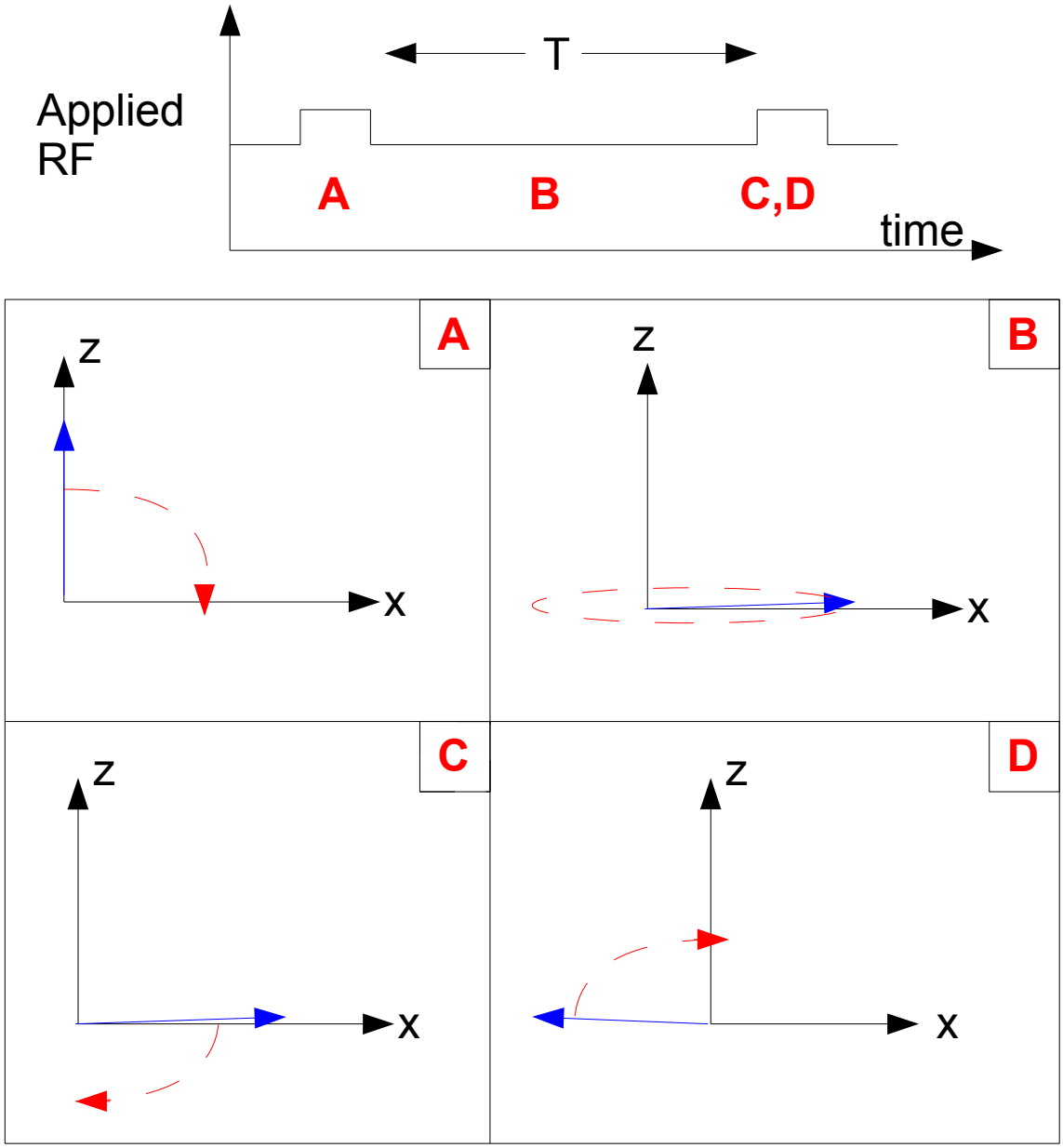

Figure 1.2: Ramsey sequence. The y-axis points into the page but has been removed for clarity. Overall pulse sequence is at the top, with the $\frac{\pi}{2}$-pulses represented by the square pulses (the square pulses are actually coherent oscillating RF fields). (A) The first $\frac{\pi}{2}$-pulse rotates the spin (blue) into the xy-plane. (B) Spin freely precesses about the z-axis (B_0 field). After free precession time T, the spin can be (C) in phase or (D) out of phase with the second $\frac{\pi}{2}$-pulse or part way between. If in phase, (C) the second $\frac{\pi}{2}$-pulse will rotate the spins down, while if it is out of phase (D) the spins will rotate up.

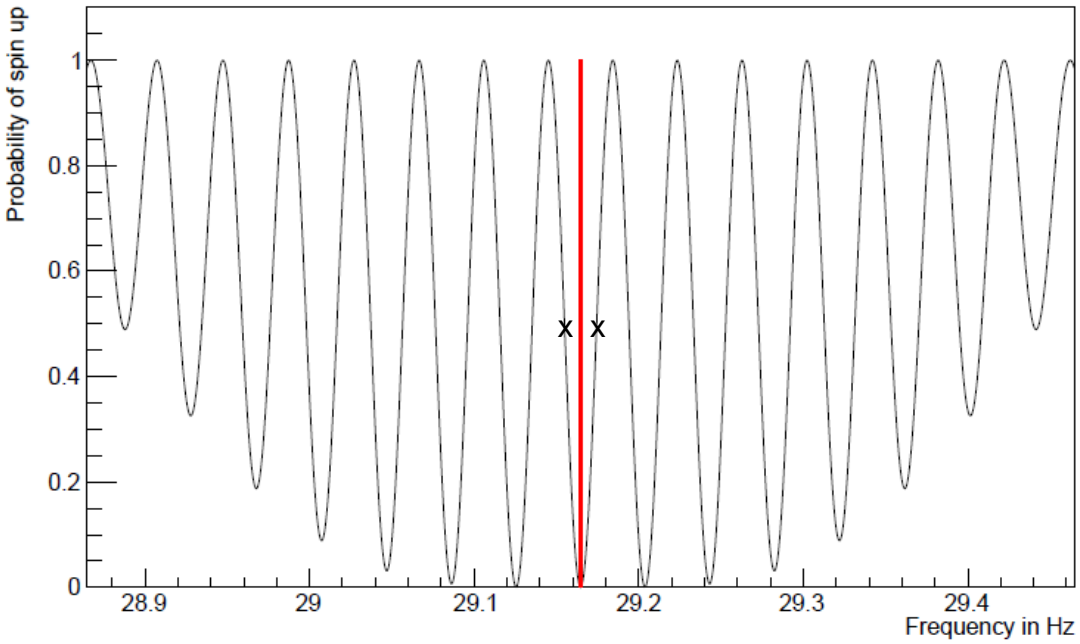

Figure 1.3: Characteristic Ramsey resonance curve showing the probability curve obtained using Equation 1.6 with $T = 23$ s and $\tau = 1$ s and varying the frequency . The resonance frequency is indicated by the red line. The y-axis is the probability of the "up" spin state and the x-axis is the frequency of the applied B_1 field. The x's at the points of greatest slope indicate experimental points.

of $m\pi$, where m is an even integer. The probability curve has the form of:

$$P_{\uparrow} = 4\sin^2\theta\sin^2\left(\frac{1}{2}a\tau\right)\left[\cos\frac{1}{2}\lambda T\cos\frac{1}{2}a\tau - \cos\theta\sin\frac{1}{2}\lambda T\sin\frac{1}{2}aT\right]^2, \tag{1.6}$$

where

$$\lambda = \omega_0 - \omega \quad , \quad a = \left[\lambda^2 + (2\left|\gamma B_1\right|)^2\right]^{\frac{1}{2}},$$
$$\sin\theta = \frac{2\left|\gamma B_1\right|}{a} \quad , \quad \cos\theta = \frac{\lambda}{a},$$

T is the free precession time (time between $\frac{\pi}{2}$ pulses) and τ is the length of the $\frac{\pi}{2}$-pulse [12]. The experiment is typically run at the point of greatest slope, as indicated by two x's in Fig. 1.3. This point is just off resonance and creates the largest change in neutron count for a small frequency change. The spins precess freely for as long a time T as possible about B_0, ultimately limited by the free neutron mean lifetime of 881 s. Experimentally, the free precession time is shorter than the free neutron decay time, and ILL measured a free precession time of $T = 130$ s.

1.2.2 Hg-199 Comagnetometer

A high degree of control for the magnetic field is necessary to achieve the desired level of precision for a nEDM measurement. Field inhomogeneities and instabilities are the major source of systematic error in the ILL n-EDM experiment. The error was mitigated by measuring the magnetic field in the experimental volume at the same time as measuring the precession frequency of the neutrons using a Hg-199 "comagnetometer". This magnetometer was unique because it allowed for a simultaneous precision measurement of both neutron precession and mercury precession.

The apparatus is shown in Fig. 1.1. The basic principle of the Hg-199 comagnetometer used in the ILL n-EDM experiment is as follows. First, the mercury atoms are polarized by optical pumping, a process described in Section 2.2. Then low pressure Hg-199 is introduced into the experimental volume at the same time as UCN. The neutrons and mercury atoms are allowed to freely precess for the same amount of time before the precession frequencies are measured. The mercury precession

frequency is measured directly using a photomultiplier tube. The frequency is found by detecting the change in optical signal due to the change of orientation of the mercury spin as it precesses. The neutrons are drained from the experimental volume and detected. While this method allows for an excellent measurement of the magnetic field, it introduces its own systematic errors into the measurement [13, 14]. The most important error, which is believed to be the dominant systematic error in future experiments, is a false EDM arising from the geometric phase effect described in Section 1.2.3.

1.2.3 Geometric Phase Effect

As the neutron travels around the cell it accrues a geometric phase which influences its precession frequency [8]. This effect on the frequency leads to a false EDM.

One example of a geometric phase arises in the Foucault pendulum [17]. While the earth rotates through an angle of 2π in one day, the pendulum precesses through an angle of $2\pi\cos\theta_0$, where θ_0 is the latitude. Since the pendulum did not return to its initial state of motion, after one complete rotation, it is said to have acquired a geometric phase.

Any particle in a trap (in ILL's case, either ^{199}Hg or UCN) is subject to the geometric phase effect. The geometric phase effect as applied to a trapped neutron is described here, but the derivation is equally valid for ^{199}Hg [13]. To explain the effect on the neutrons, I follow the arguments presented in Ref. [13].

The motion of the neutron through the electric field creates a magnetic field, $\vec{B}_v = \frac{\vec{E}\times\vec{v}}{c^2}$ in the rest frame of the neutron where $\vec{v}$ is the neutron velocity and c is the speed of light. The motional magnetic field is small compared to the main magnetic field B_0 but is of the same order as the magnetic inhomogeneities in the xy-plane of the B_0 field. Assuming cylindrical symmetry,

$$\vec{B}_{0xy} = -\left(\frac{\partial B_{0z}}{\partial z}\right)\left(\frac{R}{2}\right), \tag{1.7}$$

where R is the radius of the cylindrical trap, z is the height, $\vec{B}_{0xy}$ is the magnetic inhomogeneities in the xy-plane arising from the B_0 field and $\partial B_{0z}/\partial z$ is the magnetic inhomogeneities arising from

the gradient along the z axis.

The total field in the xy-plane $\vec{B}_{xy} = \left(\vec{B}_{0xy} + \vec{B}_v\right)$ is then a small field that approximately rotates around $\vec{B}_0$ as the neutrons circulate around the cylindrical trap. The geometric phase effect may then be considered as a Bloch-Siegert shift [18]. To first order, the Bloch-Siegert shift $\Delta\omega$ is given by [9]

$$\Delta\omega = \frac{\omega_{xy}^2}{2\left(\omega_0 - \omega_r\right)}, \tag{1.8}$$

where in applying the formulae to neutrons confined to a trap, the following symbols are defined: ω_r is the angular speed of motion of the neutrons circulating in the xy-plane and $\omega_{xy}^2 = \gamma^2 B_{xy}^2$. Thus, three terms are involved from the magnetic field, a $\vec{B}_{0xy}^2$ term, a $\vec{B}_v^2$ term and their cross term, $\vec{B}_{0xy} \cdot \vec{B}_v$. The cross term will contribute to a false EDM because it depends on the relative orientation of $\vec{E}$ with respect to $\vec{B}_0$.

The neutrons can travel in both directions in the xy-plane, designated by a $+$ for clockwise and $-$ for counter-clockwise. Since both directions are equally probable, to get the net Bloch-Siegert shift the average of both directions must be considered. This modifies Equation 1.8 to

$$\Delta\omega = \frac{\left(\gamma B_{xy+}\right)^2}{4\left(\omega_0 - |\omega_r|\right)} + \frac{\left(\gamma B_{xy-}\right)^2}{4\left(\omega_0 + |\omega_r|\right)}. \tag{1.9}$$

The horizontal fields B_{xy+} and B_{xy-} will depend on the orientation of the electric field relative to B_0. In the parallel case,

$$B_{xy+} = B_{0xy} - |B_v| \qquad \text{and} \qquad B_{xy-} = B_{0xy} + |B_v|$$

with the signs being reversed for the anti-parallel orientation. With the magnetic field $B_{xy\pm}$ being different with respect to the relative orientation of the $\vec{B}_0$ and $\vec{E}$ fields, the Bloch-Siegert shift will also be different for each. This allows us to calculate the frequency difference between the two orientations,

$$(\Delta\omega_{\uparrow\uparrow} - \Delta\omega_{\uparrow\downarrow}) = -2\gamma^2 B_{0xy}|B_v|\frac{|\omega_r|}{\omega_0^2 - \omega_r^2}. \tag{1.10}$$

This gives rise to a false EDM d_{af} given by:

$$d_{af} = -\left(\Delta\omega_{\uparrow\uparrow} - \Delta\omega_{\uparrow\downarrow}\right)\frac{J\hbar}{2E}, \tag{1.11}$$

where $J = \frac{1}{2}$ for the neutron (and Xe-129).

There are now two cases to consider, $|\omega_r| << |\omega_0|$ and $|\omega_0| << |\omega_r|$. The first case is known as the adiabatic case. This is the case for UCN. Using this approximation, $|\omega_r| << |\omega_0|$, Equation 1.10 becomes

$$(\Delta\omega_{\uparrow\uparrow} - \Delta\omega_{\uparrow\downarrow}) = -2\gamma^2 B_{0xy}|B_v|\frac{|\omega_r|}{\omega_0^2}\left[1 - \frac{\omega_r^2}{\omega_0^2}\right]^{-1}. \tag{1.12}$$

Combining Equations 1.11 and 1.12, and substituting $B_v = \frac{V_{xy}E}{c^2}$, $\omega_0 = \gamma B_{0z}$, $\omega_r = \frac{V_{xy}}{R}$ where R is the radius of the trap results in

$$d_{af} = -\frac{J\hbar}{2}\left(\frac{\partial B_{0z}/\partial z}{B_{0z}^2}\right)\frac{V_{xy}^2}{c^2}\left[1 - \frac{\omega_r^2}{\omega_0^2}\right]^{-1}. \tag{1.13}$$

The second case, $|\omega_0| << |\omega_r|$, is primarily relevant for the comagnetometer, because the atoms are at room temperature. Using the same techniques as Equations 1.12 and 1.13, the resultant false EDM is

$$d_{af} = -\frac{J\hbar}{2}\left(\frac{\partial B_{0z}}{\partial z}\right)\frac{\gamma^2 R^2}{c^2}\left[1 - \frac{\omega_0^2}{\omega_r^2}\right]^{-1}. \tag{1.14}$$

The geometric phase effect will lead to a false EDM that will depend on the velocity of the particles relative to the Larmor frequency. This is a non-trivial effect and must be accounted for in current and next generation n-EDM experiments. At ILL, the gradient field was measured and the effect was corrected for. In general a superior strategy would be to reduce the effect by controlling the relevant parameters such as the size of the gradient and the size of the cell R. Furthermore it has been suggested that reducing the mean free path of the comagnetometer atoms would reduce the false EDM. This is discussed in Section 1.2.4

1.2.4 Mitigating False EDM by Limiting the Mean Free Path

The mean free path of a gas is the average distance a particle will travel before a collision with another similar particle. High pressure gas will experience a shorter mean free path than the same gas at low pressure. Decreasing the mean free path of the comagnetometer gas suppresses its false EDM [13, 14].

The Hg-199 pressure needed to be low in the ILL experiment in part due to the neutron capture cross section of Hg-199. The original idea for using Xe-129 as an alternative to Hg-199 revolved around its lower neutron capture cross section, which therefore allowed higher pressure Xe-129 to be used, limiting the mean free path [19].

1.2.5 Xenon-129 Comagnetometer Concept

Xenon is the second heaviest noble gas with eight stable isotopes, the three most common isotopes being Xe-129 (26.4%), Xe-131 (21.2%) and Xe-132 (26.9%) where the isotopic abundance is noted in parentheses. Two stable isotopes, Xe-129 and Xe-131, have non-zero nuclear spin allowing for them to be used in nuclear magnetic resonance experiments (discussed in Chapter 3). Of these two isotopes, Xe-129 was selected due to having a nuclear spin of $\frac{1}{2}$, long T_1 relaxation times, and a long hyperpolarized lifetime (discussed in Chapter 2). The other isotope Xe-131 is generally not used because the nucleus is spin-$\frac{3}{2}$ which results in additional quadrapole relaxation mechinisms and therefore shorter spin relaxation times [15].

Isotopically pure Xe-129 has been proposed to be used as a comagnetometer in a new n-EDM experiment at TRIUMF. As mentioned in Section 1.2.4, the initial idea to use Xe-129 as a co-magnetometer was based on using it to limit false EDM effects. Xe-129 posesses a lower neutron capture cross section compared to Hg-199 therefore the number density of Xe-129 can be increased compared to Hg-199. The number density can be increased sufficiently to limit the mean free path of the xenon atoms, via interatomic collisions, to distances smaller than the cell size. Limiting the mean free path in this fashion tends to reduce the sensitivity to the geometric phase effect.

Xe-129 has a neutron capture cross section of 21 barns, compared to 2150 barns for Hg-199.

Based on this, if limited by neutron capture alone, the Xe-129 pressure could be increased as large as 5 mTorr which would give UCN lifetimes in the cell similar to the typical lifetimes of UCN in the absence of Xe-129. There are however, several other challenges related to the comagnetometer.

One such challenge is electrical breakdown. The sensitivity to the neutron EDM is directly propotional to the electric field that can be applied to the neutron. As large as possible an electric field is therefore desirable. However, the presence of low pressure gasses is known to limit the breakdown voltage according to Paschen's Law. The Paschen curve has been measured near this region of operating pressures and electrode gap [20]. These measurements indicate that lower pressure is favourable. The pressure could be as large as 0.7 mTorr. However this would have to be demonstrated experimentally for the TRIUMF experiment.

Another challenge is signal. For 0.7 mTorr Xe-129, the signal in a loop connected to a SQUID placed beneath the ground plate of the n-EDM cell is anticipated to sense a 10 fT signal. This remains one possible plan for detection if the pressure can be kept large enough.

The original idea of Xe-129 was to use Xe-Xe collisions to reduce the mean free path to reduce the false EDM arising from the geometric phase effect. It has been noted that the estimated mean free path used in Ref. [19] was nearly ten times too small. At 0.7 mTorr and using the correct mean free path, it is unlikely that the false EDMs induced by the geometric phase effect would be reduced [21].

There are possible solutions to these issues. Other buffer gasses could be used with superior neutron capture and electrical breakdown properties such as helium and nitrogen, which could also mitigate the geometric phase effect. It is also possible that different RF sequences could be used to modify the geometric phase effect [22, 23]. The best solution for coping with the small signal is a system based on two photon excitation [24], which is being pursued by collaborators at the University of British Columbia. Our group is responsible for the polarized xenon source whereas the UBC group's responsibility is the detection of the polarization within the EDM cell. The two photon technique relies on probing Xe-129 hyperfine structure with XUV laser light.

1.3 Neutron EDM Experiment at TRIUMF

A next generation electric dipole moment experiment will be the flagship experiment for the new high density UCN source at TRIUMF. The UCN source is presently being developed at the Research Centre for Nuclear Physics (RCNP) in Osaka, Japan. Neutrons liberated from a spallation target by an incident proton beam are moderated in materials to become cold neutrons. The cold neutrons become UCN via downscattering (phonon emission) in a bath of superfluid He at 0.8 K.

In contrast, the UCN source at ILL uses neutrons produced in a reactor that have been moderated down to cold levels. Cold neutrons (speed $v = 50$ m/s) then reflect off a neutron turbine [25] losing kinetic energy to become ultracold ($v < 9$ m/s). This setup achieved 0.7 UCN/cm^3 in the EDM cell, as mentioned in Section 1.2. At TRIUMF, the UCN source is expected to deliver 1200 polarized UCN/cm^3 to the experimental cell [26], which will reduce statistical errors. The combination of the spallation source and the use of superfluid helium in the UCN source that give rise to this expectation. The goal of the experiment at TRIUMF is to constrain the neutron EDM on the order of 10^{-27} e $\cdot$ cm in initial runs to prior to 2018. Improvements to the setup would result in an improved precision to the 10^{-28} e $\cdot$ cm level after 2018.

A n-EDM experiment using a Xe-129 comagnetometer has been proposed at TRIUMF as discussed in Section 1.2.5. This requires a source of hyperpolarized Xe-129.

1.4 Thesis Overview

This thesis focuses on construction and testing of a flow through Xe-129 polarizer. The polarizer features a 75 W diode laser combined with a gas feed system and rubidium optical pumping cell. Nuclei of Xe-129 became polarized in the cell via spin exchange collisions with rubidium. The hyperpolarized xenon was transported through a plastic tube from the polarizer setup to an adiabatic fast passage nuclear magnetic resonance (AFP-NMR) setup for characterization. Adiabatic fast passage experiments were performed to characterize the net polarization and Xe spin relaxation. The present status and experimental results from the new system are reported. This thesis will

review progress towards the eventual system for nEDM experiments where polarizations greater than 50% and T_1, T_2 relaxation times greater than 1000 s are expected.

Chapter 2

Hyperpolarized Xenon Production

2.1 Introduction

Hyperpolarized noble gases are atomic systems whose polarization is typically multiple orders of magnitude larger than the thermal polarization. Hyperpolarization may be produced via spin exchange optical pumping. The full valence shell allows for spin-polarization to be transferred directly to the nucleus, as discussed in Section 2.3. Furthermore, noble gas nuclei typically have long relaxation times [29].

Two isotopes, He-3 and Xe-129, have been typically studied over other noble gas nuclei because of their use in medical imaging [29, 30]. In particular, Xe-129 has favourable properties considering its possible use as a comagnetometer, as discussed in Section 1.2.5.

Spin exchange optical pumping (SEOP) [29, 31, 32, 33] is a two-step process. First, an alkali metal (usually rubidium (Rb)) is optically pumped by circularly polarized light into a hyperpolarized dark state. A dark state is an atomic state that does not absorb light due to selection rules. Once this state has become populated, the Rb atomic polarization is transferred to the nucleus of xenon through a Fermi contact process known as spin-exchange. Both processes are described below.

2.2 Optical Pumping

Rubidium has a ground state electronic configuration of $1s^2 2s^2 2p^6 3s^2 3p^6 3d^{10} 4s^2 4p^6 5s^1$. It has one valence electron, in the $5s$ orbital, in the ${}^2s_{1/2}$ state. This letter notation is known as spectroscopic notation and has the form ${}^{2S+1}\ell_J$, with ℓ denoted by the letters given in Table 2.1. For example, an electron in the ${}^2s_{1/2}$ state has a spin S of $\frac{1}{2}$, orbital angular momentum ℓ of 0 and a total electronic angular momenum J of $\frac{1}{2}$.

Letter values of ℓ.	
ℓ	Letter Value
0	s
1	p
2	d
3	f
4	g

Table 2.1: Letter values of ℓ. Higher values follow alphabetically after g.

Optical pumping is used to excite atomic transitions in Rb. The D1 transition line of Rb-85 and Rb-87 (in natural abundance) is used for our optical pumping setup, as commonly done in SEOP setups. We describe here the states relevant to Rb-85; the analogous discussion for Rb-87 is slightly different because of the difference in nuclear spin. The D1 transition is from the electronic ground state of ${}^2s_{1/2}$ to the excited state ${}^2p_{1/2}$. An unpolarized photon has an angular momentum of $\ell = 1$ and magnetic quantum number $m = -1, 0, \text{or} + 1$. During an electronic transition from the ${}^2s_{1/2}$ to the ${}^2p_{1/2}$ state using an unpolarized photon, the electron can move to any of the different m states, obeying the selection rule $\Delta m = -1, 0, +1$. Likewise during relaxation it can relax into any of the available m states.

Hyperfine splitting accounts for coupling between nuclear spin (I) and total electronic angular momentum (J), and splits both the $5s_{1/2}$ and $5p_{1/2}$ into two non-degenerate states labeled by F. Rubidium-85 has a nuclear spin of $I = \frac{5}{2}$ leading to two hyperfine states $F = 2$ and $F = 3$. Both hyperfine states will be excited by our laser because the energy difference ($\lesssim 10$ GHz) between the two hyperfine states is small, compared to Doppler broadening ($\sim$ GHz) and the width (~ 150 GHz) of our diode laser. We purposely pressure broaden the Xe pressure to 50 PSI to increase the width

of the D1 transition line to $\gtrsim 200$ GHz to ensure full absorption of the laser light.

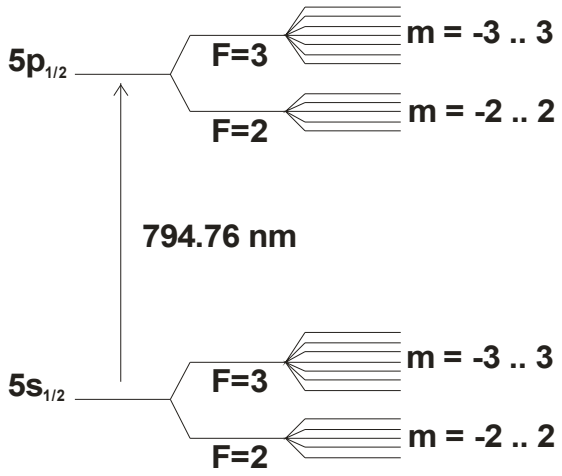

Figure 2.1: Relevant energy levels of Rubidium-85 (Not to scale). The D1 transition is shown, along with hyperfine and Zeeman splitting for each level. The F splittings are 3035.7 MHz for the $5s_{1/2}$ level and 361.5 MHz for the $5p_{1/2}$ level. The m splittings depend on the magnetic field and are therefore schematic and indicative of the weak field limit. The D1 transition wavelength is given in air [34].

In the presence of a small static magnetic field each hyperfine state is further broken into $2F + 1$ energy states via Zeeman splitting as illustrated in Figure 2.1. The energy difference between these states is even smaller than the hyperfine difference, and all are available for excitation. The different energy states are split according to the magnetic quantum number. In this case, each hyperfine state will have Zeeman states with $m = (-F, -F + 1, ..., F - 1, F)$. Without a magnetic field present, these states would all be degenerate.

Thermally, all ground electron states ($5s_{1/2}$) are equally populated. Using right circularly polarized (σ^+) light and a properly aligned magnetic field, a transition value of $\Delta m = +1$ can be selected. This restriction forbids any transition from the ground state of $m = 3$, since no $m = 4$ excited state exists. The electron can freely move between hyperfine states, i.e. $F = 2$ to $F = 3$, because the selection rules require that $\Delta F = 0, \pm 1$. Any electrons that are able to be excited, i.e. electrons with $m = -3, -2, -1, 0, +1, +2$, absorb the photon and move to the relevant state. These electrons may now relax freely (via photon emission) to any m state provided that $\Delta m = 0, \pm 1$. Photons emitted during relaxation are absorbed as rotational or vibrational energy by a buffer gas, typically helium or nitrogen, rather than being absorbed by pumped rubidium atoms (which would lead to

a net decrease in polarization) [30, 35].

Repeated optical transitions and relaxations therefore leads to a buildup of rubidium atoms with their valence electron in the ground state with $F = +3$ and $m = +3$. At this point, the rubidium has non-thermal population saturation in this state, achieving the distinction of hyperpolarized rubidium. This provides the hyperpolarized sample of rubidium necessary for hyperpolarizing xenon.

2.3 Spin Exchange

Hyperpolarized xenon is created through spin exchange collisions with polarized alkali-metal, such as Rb. The metal atoms are polarized through optical pumping, as discussed in Section 2.2. Spin exchange between alkali-metals and heavy noble gases is achieved through interactions within van der Waals molecules. Efficient spin exchange requires the alkali metal (typically rubidium-85), a heavy noble gas (xenon-129) and a buffer gas whose presence is crucial in the spin exchange process. This buffer gas is usually nitrogen, helium or a mix of the two.

As shown in Figure 2.2, through a three body collision involving Rb, Xe and N_2, a Xe-Rb van der Waals molecule is formed [36]. The Xe-Rb molecule is broken after another collision with N_2. During the lifetime of the van der Waals molecule, spin can be transferred via the Hamiltonian

$$H = A\vec{I} \cdot \vec{S} + \gamma\vec{N} \cdot \vec{S} + \alpha\vec{K} \cdot \vec{S},$$

where A, γ and α are parameters representing the strength of angular momentum exhange reactions, $\vec{I}$ is the nuclear spin of rubidium, $\vec{S}$ is the electronic spin of rubidium , $\vec{N}$ is the rotational angular momentum of the Xe-Rb atom and $\vec{K}$ is the nuclear spin of xenon. The first term $A\vec{I}\cdot\vec{S}$ is a magnetic dipole interaction between the Rb electronic spin and Rb nuclear spin. The second term is a spin-rotation interaction between the rubidium electronic spin and the rotational angular momentum of the van der Waals molecule. The last term of the Hamiltonian $\alpha\vec{K} \cdot \vec{S}$ is the most important for hyperpolarization, because it gives the mixing of the nuclear spin of the xenon with the electronic spin of the rubidium via a magnetic dipole interaction.

Because of this term, the Xe nucleus may become hyperpolarized via spin-exchange collisions

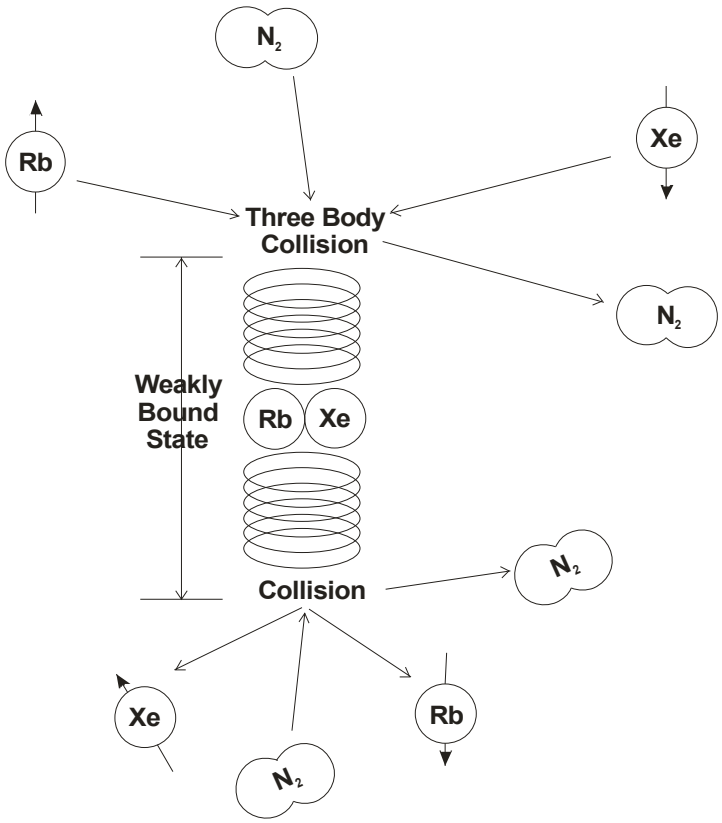

Figure 2.2: Spin exchange between polarized rubidium and unpolarized xenon. The nitrogen present in the buffer gas allows for the creation of a Xe-Rb van der Waals molecule through three-body collisions. The van der Waals molecule lasts until it is struck by another atom or molecule in the mixture. The rubidium electron spin and xenon nuclear spin are both weakly coupled with the rotational angular momentum of the molecule in this state with some of the polarization (< 10 %) being transfered from the rubidium electron spin to the xenon nucleus. The rest is lost as rotational energy to the van der Waals molecule (represented by the elipses). [36]

with the hyperpolarized Rb. The degree of polarization achievable by the Xe is limited by a variety of experimental parameters [36], many of which are studied in this thesis and presented in greater detail in Chapter 4.

2.4 Experimental Setup

The experimental setup at the University of Winnipeg is designed to be a continuous flow system consisting of a laser with associated optics and a gas flow system. The setup was originally designed and used at the National Research Council Steacie Institute for Molecular Sciences (NRC-SIMS), in Ottawa [37, 38]. An overview of its operation is given here with further details given in Sections 2.4.1 - 2.4.3.

The polarizer consists of two main components: an optics system and a gas system. A schematic diagram of the apparatus is shown in Figure 2.3. Beginning with the laser, light is produced and exits through a fibre before being collimated by a lens. The beam enters a polarizing beam cube and a quarter wave plate. This produces circularly polarized light which enters the spin exchange optical pumping cell. In the SEOP cell, rubidium vapor absorbs the circularly polarized light and through collisions produces hyperpolarized xenon via spin exchange, as described in Section 2.3. The xenon gas mixture flows upstream against the direction of the incident laser light.

The gases are pre-mixed and stored in a high-pressure cylinder. Before entering the cell the gas is regulated to the desired operating pressure, purified (using seperate moisture and oxygen traps), and monitored with a flow meter and a pressure gauge. The temperature of the SEOP cell area (T_C) and the rubidium reservoir (T_R) are controlled with heater tape and monitored with a digital thermometer.

2.4.1 Laser and Optics

Our laser is a QPC BrightLock Ultra-100 laser that provides 795 nm wavelength light with a 75W diode module output through a 600 μm fiber. The laser provides an intense beam that is tunable over a 2 nm range by specifying laser current and the base cooling temperature. The laser current

is controlled by a LDX-3690 High Power Laser Diode Current Source. Cooling is provided by an Ultra-therm water-cooled chiller and a cooling plate upon which the laser head is mounted. Relevant laser parameters were characterized and the results are presented in Section 4.1.

The laser and cooling plate are mounted on a custom designed acrylic housing. The output fiber is attached to a lens tube containing a collimator lens (Thor Labs LA1131-B) to produce a one inch diameter beam. The laser light begins linearly polarized but loses polarization as it travels through the fibre. To fix this issue, the beam passes through a polarizing beam cube (Newport 10BC16PC.6). The majority (89 percent) of the power is transmitted through the cube into a quarter wave plate (Thor Labs WPQ10M-780) and on to the spin-exchange optical pumping cell. The remainder of the beam is diverted 90° and monitored for power output using a Newport model 1918-C power meter. The laser and all optics are mounted on a separate aluminum plate that is on a vertical positioning system, as shown in Fig. 2.6. This allows for fine tuning of the vertical position of the beam relative to the SEOP cell, while ensuring that all optics are rigidly attached.

A spectrometer is used to monitor the laser beam during operation. The spectrometer is an Ocean Optics Jaz module with the following specifications: grating "six"(diffraction grating centred on 750 nm with a spectral range of 200-270 nm), and a 5 μm slit. The spectrometer is also used as a first indication of optical pumping. Once a sufficient quantity of rubidium vapour builds up in the SEOP cell the laser light cannot penetrate the cell, provided that the solenoid surrounding the cell is off. With all the laser light being absorbed, the laser's spectral peak disappears from the spectrometer. However, once the solenoid is turned on, optical pumping takes place. Once most of the rubidium has been pumped to the dark state (as explained in Section 2.2) the cell becomes transparent to the incident laser light resulting in a renewed peak observed on the spectrometer. By observing the peak on the spectrometer while turning the magnetic field of the solenoid on and off, as shown in Fig. 2.4, the effect of optical pumping of Rb can be observed.

2.4.2 Spin Exchange Optical Pumping Cell

The spin exchange optical pumping cells were custom made by Stephen Lang and Mike Vandenhoff at NRC-SIMS using the procedure described in Ref. [37]. The cell itself consists of three parts:

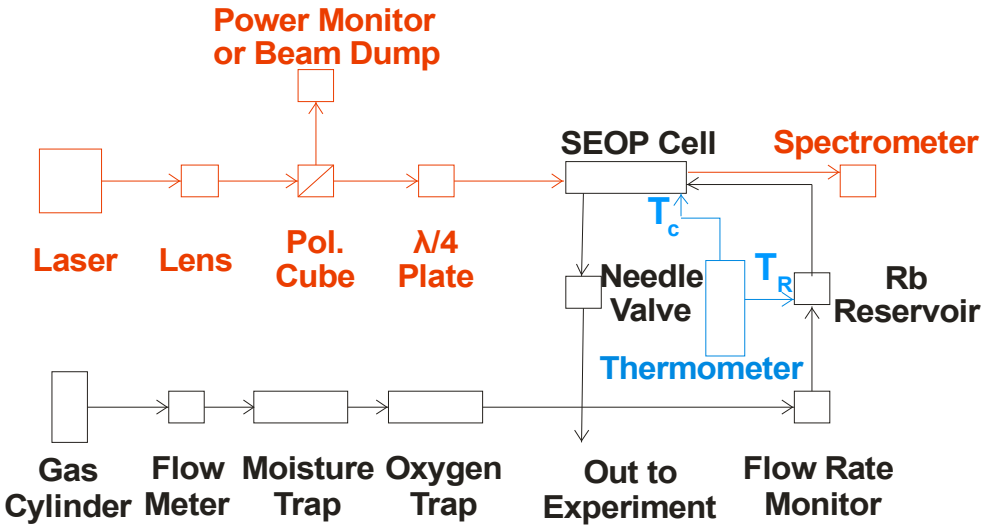

Figure 2.3: Schematic diagram of the principle operation of the University of Winnipeg Xe polarizer. Optical path is shown in red, physical gas flow path is shown in black. The SEOP cell and Rb reservoir temperatures are indicated by T_C and T_R respectively.

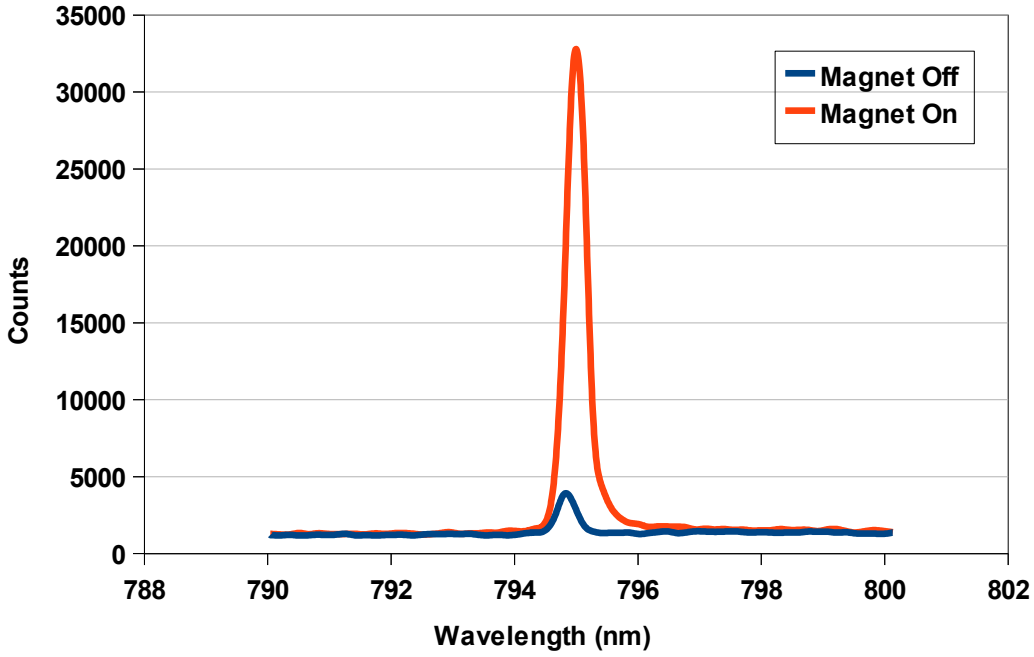

Figure 2.4: The signal detected by the spectrometer when the solenoid is on and off. Vertical units are counts which is proportional to the number of photons sensed by the detector (nominally 41 photons/count at 600 nm according to the manufacturers specifications). The magnet off state gives the smaller signal while the magnet on state gives the larger signal. The difference seen is due to optical pumping when the magnetic field is present, providing a quantization axis for the Zeeman sublevels in the Rb atoms.

a Rb reservoir, an SEOP cell and an exit guide. A picture of the glassware may be seen in Fig. 2.5. The rubidium reservoir is heated to 200 °C to liquify the Rb and hence increase its vapour pressure, so that the gas mixture flowing past will carry a sufficient concentration of Rb atoms into the spin exchange area. The Rb reservoir is wrapped in heater tape and temperature controlled by setting a voltage percentage on a Variac monitoring the temperature with a digital thermometer (Omega HH22A). The spin exchange area is located between two relatively flat glass faces, forming a cylinder. Within the cylinder is the region where the optical pumping and spin exchange takes place. The SEOP cylinder and exit guide are coated in SurfaSil (available from Pierce Scientific). SurfaSil is a siloxane that reduces surface-induced relaxations of the Xe polarization [37]. During optical pumping, a solenoid placed around the SEOP provides the necessary magnetic field ~ 1 mT. Further details of the design and treatment of the cell are given in Ref [37].

2.4.3 Flow Through Gas System

Gas is provided in a high pressure cylinder from AIRLIQUIDE with a composition of 1.00% Xe, 2.92% N_2, balance He (96.08%) by molar concentration [39]. The exact ratio used at the University of Winnipeg is noted here because the xenon concentration is vital to calculating the polarization (Section 4.4). The exact ratio of gases, however, is not critical to the spin exchange process. Typical ranges are from 1% to 3% Xe and 1% to 10% N_2 with the balance being He [40, 41].

The gas is regulated to the desired experimental pressure using a regulator on the gas cylinder. Before entering the SEOP cell the gas passes through a pressure meter (Union Carbide 400 psi), an oxygen trap (Chromatography Research Supplies Model 1000), a moisture trap (Matheson Gas Products C427-45), and a flow gauge (Omega FMA-A2307) calibrated for helium. The oxygen and moisture traps remove any remaining oxygen and water that may be present in trace amounts. After the SEOP cell, some glass wool is placed in the tubing after the exit valve from the SEOP cell to stop any stray rubidium from leaving the cell. The flow rate is controlled by a needle valve placed between the SEOP cell and the experimental bottle in the AFP NMR setup (described in Chapter 3). The bottle has a small hole in the cap allows some hyperpolarized xenon to build up in the experimental area while still allowing flow to occur.

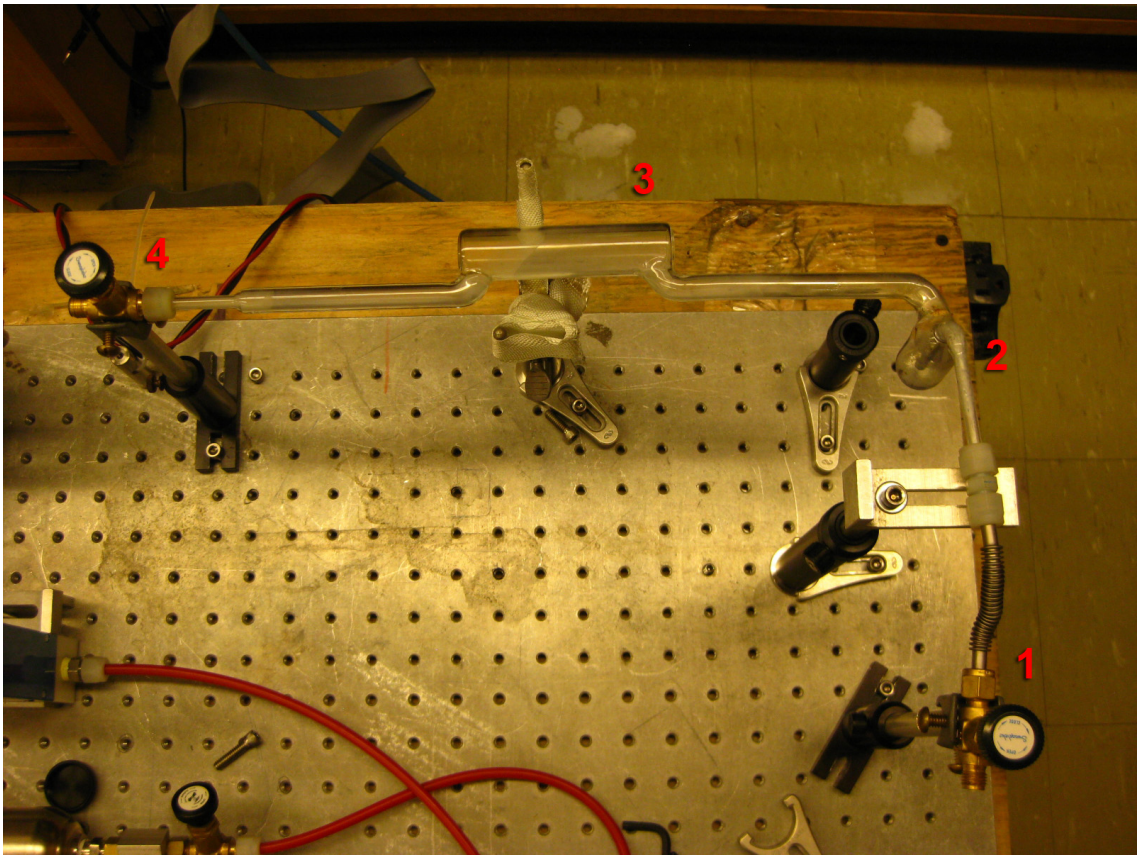

Figure 2.5: An optical pumping cell during installation. The total cell length (left to right) is 37 cm long. The gas mixture containing Xe enters at the bottom right (1) and mixes with rubidium from the rubidium reservoir (2). The optical face of the SEOP cell (3) is 32 mm OD. Spin exchange takes place in this region and exits the cell at the top left (4). The ends of the cell are sealed by two Swagelok brass valves.

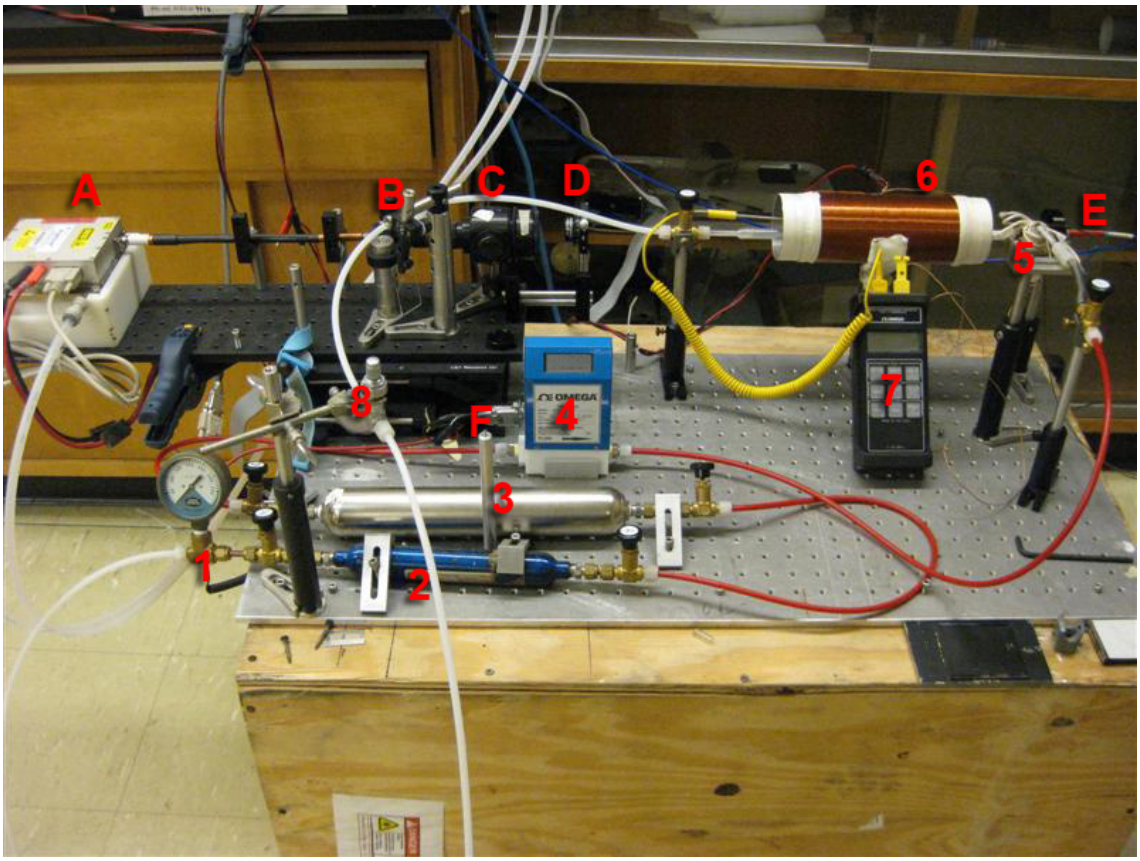

Figure 2.6: Flow through gas system setup. Gas enters through the line at the lower left (1). The pressure meter (1), gas traps (2,3) and flow meter (4) are installed on the laser breadboard. The rubidium cell (5) is located before the SEOP cell (which is contained inside the solenoid (6)) at the top right of the picture, behind the thermometer (7). The laser is visible at the extreme left (A) off the table on its own breadboard, which is in turn mounted on a vertical translation stage. All optics (B,C,D) are mounted on the laser breadboard. The spectrometer is on the far right of the picture (E). The power meter/beam dump has been removed; it is normally installed on the empty post located between the two gas traps during operation (F). Hyperpolarized xenon exits the system through the needle valve, visible above the gas traps (8). The needle valve controls the flow rate of the system.

Chapter 3

Polarization Detection using Nuclear Magnetic Resonance

3.1 Introduction

Nuclear magnetic resonance (NMR) is a physical phenomenon that occurs with nuclei with non-zero spin. The NMR technique involves magnetic fields acting on a nucleus causing its spin to precess at a specific frequency. NMR has many useful applications, the two most well known being chemical NMR spectroscopy, and magnetic resonance imaging (MRI). These techniques exploit the dependence of the resonant frequency on the static field strength.

Contrary to typical NMR and MRI experiments, low magnetic fields are used in our experiment. In typical NMR experiments, nuclei are polarized by a strong (≥ 1 T) magnet. Conventional NMR uses this high magnetic field strength to produce a polarized sample through Boltzmann (thermal) polarization. Low field NMR [42] on the other hand often requires different methods of polarization to achieve sufficient signal.

Hyperpolarization (described in Chapter 2) boosts the polarization far beyond thermal values, removing the need for powerful magnets for polarization. The NMR experiment can then be conducted in lower magnetic fields, with resonant frequencies of tens of kHz or lower (compared to the tens to hundreds of MHz for traditional NMR experiments running in high magnetic fields). In the

case of xenon, hyperpolarization is achieved through SEOP as discussed in Chapter 2.

The University of Winnipeg polarizer produces hyperpolarized Xe-129. The polarized gas that is produced is analyzed using NMR. The relevant NMR techniques are briefly described in this section. Further details can be found in several textbooks [48, 46].

3.1.1 Introduction to NMR

Consider a stationary nucleus with magnetic moment $\vec{\mu}$ interacting with a magnetic field $\vec{B}$. The Hamiltonian is

$$H = -\vec{\mu} \cdot \vec{B} = -\gamma \vec{I} \cdot \vec{B}, \tag{3.1}$$

with $\vec{\mu} = \gamma \vec{I}$ and $\vec{I}$ being the nuclear spin operator, and γ is the gyromagnetic ratio of the nuclei. The quantum mechanical state evolves according to the Schrödinger equation, resulting in the following Ehrenfest theorem for the average spin:

$$\frac{d}{dt}\left\langle \vec{I} \right\rangle = \frac{1}{i\hbar}\left\langle \left[\vec{I}, H\right] \right\rangle = \gamma \left\langle \vec{I} \right\rangle \times \vec{B}. \tag{3.2}$$

From now on drop the $\langle\ \rangle$ brackets and interpret $\vec{I}$ as the spin vector as a semi-classical approximation. Equation 3.2 then becomes:

$$\frac{d}{dt}\vec{I} = \gamma \vec{I} \times \vec{B}. \tag{3.3}$$

3.1.2 Larmor Precession

Consider a nuclear magnetic moment $\vec{\mu}$ interacting with a static magnetic field $\vec{B} = B_0 \hat{k}$. Solving Equation 3.3 gives

$$I_x = \left|\vec{I}\right| \sin\alpha \cos\omega_0 t, \tag{3.4}$$

$$I_y = -\left|\vec{I}\right| \sin\alpha \sin\omega_0 t, \tag{3.5}$$

$$I_z = \left|\vec{I}\right| \cos\alpha, \tag{3.6}$$

where t is time, α is the angle $\vec{I}$ makes with the z-axis and $\omega_0 = \gamma B_0$. This set of equations describes precession with angular velocity ω_0 around the B_0 field axis (typically the z-axis). Precession about an external magnetic field is known as Larmor precession and ω_0 is known as the Larmor (angular) frequency.

3.1.3 Probability Measurement

For spin-$\frac{1}{2}$ particles, the act of measurement in quantum mechanics is related to the projection of the mean spin vector onto the relevant axis. This can be seen by considering a measurement of the z-component of the average spin vector I_z for a spin-$\frac{1}{2}$ nuclei:

$$I_z = \frac{\hbar}{2}\left(P_{m=+\frac{1}{2}} - P_{m=-\frac{1}{2}}\right). \tag{3.7}$$

Here $P_{m=+\frac{1}{2}}$ is the probability of finding the particle in the spin up $m = +\frac{1}{2}$ state and $P_{m=-\frac{1}{2}}$ is the probability of finding the particle in the spin down $m = -\frac{1}{2}$ state. These are the only two possible m states for a spin-$\frac{1}{2}$ particle so the total probabilty must be unity:

$$P_{m=+\frac{1}{2}} + P_{m=-\frac{1}{2}} = 1. \tag{3.8}$$

Combining these equations gives the probability that the particle is in each spin state as

$$P_{m=-\frac{1}{2}} = \frac{1}{2} - \frac{1}{\hbar}I_z, \tag{3.9}$$

$$P_{m=+\frac{1}{2}} = \frac{1}{2} + \frac{1}{\hbar}I_z. \tag{3.10}$$

Thus, the probability of each state can be found from the semiclassical I_z component of the nuclear spin.

3.1.4 Nuclear Magnetic Resonance

Now consider the effect of an additional small, rotating magnetic field of magnitude B_1 in the xy-plane. The total magnetic field is

$$\vec{B} = B_0\hat{k} + B_1\cos(\omega t)\hat{i} - B_1\sin(\omega t)\hat{j}.$$

Equation 3.3 is solved for this magnetic field and the result used to find the probability of finding the nuclei in various spin states.

Using Equation 3.3 with this input magnetic field, the time evolution of the semi-classical spin vector $\vec{I}(t)$ may be solved. Suppose the initial-state spin vector is taken to be $\vec{I}(t=0) = (0, 0, \frac{\hbar}{2})$. If Equation 3.3 is then solved the result for $I_z(t)$ may be used to find the probability of a transition from the spin up state to the spin down state via Equation 3.9 [46]

$$P(t) = \frac{1}{2} - \frac{1}{\hbar}I_z(t) = \frac{(\gamma B_1)^2}{(\gamma B_1)^2 + (\omega - \omega_0)^2}\sin^2(\omega'\frac{t}{2}), \tag{3.11}$$

where $\omega' = \left[(\omega - \omega_0)^2 + (\gamma B_1)^2\right]^{\frac{1}{2}}$. This probability function has a line shape of a Lorentzian with a maximum at the resonance frequency ω_0. The quantity γB_1 is often referred to as the NMR line width. Solving Eq. 3.3 can be greatly simplified by switching coordinate systems to the rotating frame coordinate system, which is discussed in Section 3.1.5.

Consider a B_1 field at resonance with $\omega = \omega_0$. Equation 3.11 reduces to

$$P(t) = \sin^2(\frac{\gamma B_1 t}{2}) = \frac{1}{2}\left(1 - \cos\gamma B_1 t\right). \tag{3.12}$$

Assume the magnetization begins in the up state, aligned with the positive z-axis, and consider the time required to flip the spin into the xy-plane (a $\frac{\pi}{2}$-rotation). A spin in the xy-plane can be considered by setting $P(t) = \frac{1}{2}$. Solving, we find

$$t_{\frac{\pi}{2}} = \frac{\pi}{2\gamma B_1}. \tag{3.13}$$

If a B_1 field is on for this amount of time it is known as a $\frac{\pi}{2}$-pulse.

3.1.5 The Rotating Frame

The rotating frame coordinate system is a frame that rotates around the z-axis aligned with the rotation if the B_1 field. Following Ref. [45], in a coordinate system rotating with angular velocity $\vec{\omega} = -\omega\hat{k}$, derivatives with respect to time are modified according to

$$\frac{d\vec{I}}{dt} = \frac{\partial\vec{I}}{\partial t} + \vec{\omega} \times \vec{I}, \tag{3.14}$$

where $\frac{d}{dt}$ indicates that the time-derivative is taken with respect to fixed axes defined in the lab frame and $\frac{\partial}{\partial t}$ indicates that the time-derivative is taken with respect to rotating axes in a rotating frame whose origin is taken to be at the site of the nucleus is question. Using the result of Equation 3.3 and rearranging gives

$$\frac{\partial\vec{I}}{\partial t} = \gamma\vec{I} \times \left(\vec{B} + \frac{\vec{\omega}}{\gamma}\right). \tag{3.15}$$

This is identical to Equation 3.3 with the exception of an added $\frac{\vec{\omega}}{\gamma}$ term. Defining $\vec{B}_{eff} = \vec{B} + \frac{\vec{\omega}}{\gamma}$ as the effective field in the rotating coordinate system gives

$$\frac{\partial\vec{I}}{\partial t} = \gamma\vec{I} \times \vec{B}_{eff}. \tag{3.16}$$

The net effect of switching to the rotating coordinate system is therefore that the spin precesses about the effective field $\vec{B}_{eff}$, depicted in Figure 3.1. In NMR it is generally easier to consider $\vec{B}_{eff}$ in the rotating coordinate system, and we return to this in Section 3.2

3.1.6 Macroscopic Considerations: the Bloch Equations

Upon expanding from a microscopic view to a macroscopic collection of nuclei, the magnetic moment vector becomes the net magnetization $\vec{M}$ which is defined as the sum over the individual nuclear

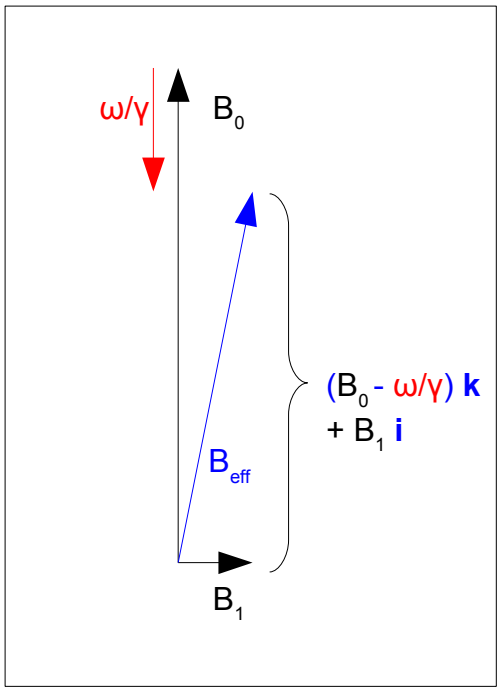

Figure 3.1: Definition of the effective magnetic field in the rotating frame. The physical magnetic fields are B_0 and B_1 (black). The rate of angular rotation is $\vec{\omega} = -\omega\hat{k}$ (red). The effective magnetic field B_{eff} is shown in black.

magnetic moments $\sum \vec{\mu_i}$. With only one NMR active nucleus in the system, Equation 3.3 becomes

$$\frac{d\vec{M}}{dt} = \gamma \vec{M} \times \vec{B}. \tag{3.17}$$

In realistic conditions, relaxation mechanisms exist. In general, these mechanisms drive the bulk magnetization vector to align with the static field $B_0\hat{k}$ with asymptotic Boltzmann magnetization M_0. For hyperpolarized systems, the value of M_0 is essentially zero, since the Boltzmann magnetization is much smaller than the hyperpolarization of the sample. Relaxation therefore generally destroys the polarization in hyperpolarized systems.

The relaxation is characterized empirically by two relaxation times: a longitudinal or spin-lattice (T_1) relaxation time and a transverse or spin-spin (T_2) relaxation time. In the presence of relaxation, the magnetization vector obeys the Bloch equations [47]:

$$\frac{dM_z}{dt} = \gamma \left(\vec{M} \times \vec{B} \right)_z + \frac{M_0 - M_z}{T_1}, \tag{3.18}$$

$$\frac{dM_x}{dt} = \gamma \left(\vec{M} \times \vec{B} \right)_x - \frac{M_x}{T_2}, \tag{3.19}$$

$$\frac{dM_y}{dt} = \gamma \left(\vec{M} \times \vec{B} \right)_y - \frac{M_y}{T_2}. \tag{3.20}$$

Considering the time evolution of M_z in Equation 3.18, the magnetization will precess around the magnetic field while it relaxes back to equilibrium value M_0 as shown in Fig. 3.2. This relaxation is characterized by T_1 and is caused by interactions between the magnetization and normal thermal motions of nearby molecules. After enough time has passed, thermal equilibrium between the magnetization and the surroundings is restored.

The transverse T_2 relaxation time is a measure of how long the individual nuclei forming the net magnetization take to dephase. Fig. 3.3 shows the transverse T_2 relaxation time. This type of relaxation can be caused by interactions between the individual spins. Due to this, T_2 is also known as the spin-spin relaxation time. An effective transverse relaxation time (sometimes called T_2^*) can be caused by magnetic field inhomogeneities across the sample volume, resulting in some

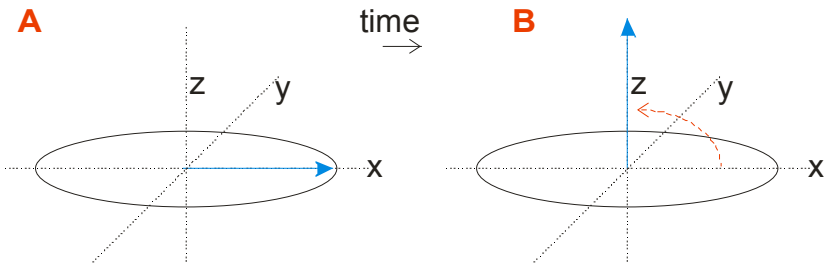

Figure 3.2: A diagram of the T_1 relaxation process. Initially spin precesses in the xy-plane. T_1 characterizes the time for the spin to relax back to the z axis (aligned with the B_0 field).

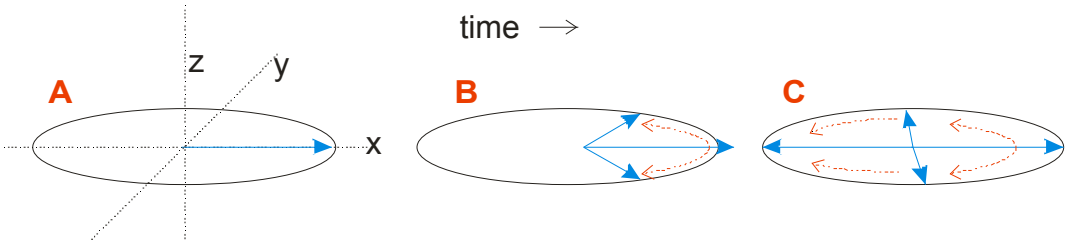

Figure 3.3: A diagram of the T_2 relaxation process. (A) Individual spins begin aligned together after being flipped into the x-y plane. (B) As the atoms move around the experimental volume each atom experiences slightly different magnetic fields, generally due to magnetic field inhomogeneities, and begins to dephase from the net magnetization direction. (C) After enough time has passed, characterized by the T_2 time constant, no signal remains as the atomic spins have dephased.

nuclei precessing faster than others. This eventually leads to a randomization of phases within the sample, and therefore a loss in transverse magnetization.

3.2 Adiabatic Passage

In NMR, adiabatic passage refers to a slow enough rate of change of the magnetic field such that, semi-classically, the magnetization angle remains constant relative to the magnetic field [48]. Quantum mechanically, adiabatic passage refers to the state preserving its magnetic quantum number when quanitized relative to the local magnetic field [45]. Strict adherence to adiabatic conditions is used to transport and analyze the polarization of Xe produced by the polarizer. We rely on adiabatic slow passage during transport of hyperpolarized Xe-129 from the SEOP cell to the experimental cell; i.e., the spin must remain aligned with the local magnetic field as the atom moves . Adiabatic fast (or rapid) passage is used to rapidly reverse the polarization within the experimental

cell for both polarization and T_1 measurements. Adiabatic slow passage and adiabatic fast passage are described separately below.

3.2.1 Adiabatic Slow Passage

To analyze the appropriate conditions for adiabaticity, consider a $\vec{B}$ field rotating in the xy-plane with angular velocity $-\omega\hat{k}$ (i.e. $B_0 = 0$) and select $\vec{I}$ to be parallel to $\vec{B}$ at time $t = 0$. Selecting a rotating frame aligned to this field, and using Eq. 3.15, the spin will precess about the effective magnetic field,

$$\vec{B}_{eff} = B_1\hat{i} + \left(\frac{-\omega}{\gamma}\right)\hat{k}. \tag{3.21}$$

If $\frac{\omega}{\gamma} << B_1$, then $\vec{B}_{eff} \approx B_1\hat{i}$ and the spin will remain staticly aligned with the x axis in the rotating frame. Transforming back to the non-rotating frame, the spin will rotate and remain aligned with the rotating $\vec{B}$ field. The spin is said to adiabatically follow the field. The adiabatic condition may be written as

$$|\omega| << \gamma B_1, \tag{3.22}$$

or, for a general time-varying magnetic field $\vec{B}(t)$

$$\left|\frac{d\vec{B}}{dt}\right| << \gamma B^2. \tag{3.23}$$

Thus, this condition requires that the direction of the magnetic field (i.e. rotation of the field ω) vary slowly compared to the local Larmor precession frequency (γB_1). If this condition is met the xenon nuclei will maintain their polarization along the field and is the mechanism responsible to get from the SEOP cell to the NMR spectrometer.

3.2.2 Adiabatic Fast Passage

Consider a weakly time-dependent magnetic field $B_0(t)$ oriented along the z-axis along with a B_1-field rotating in the xy-plane with angular velocity $-\omega$. At $t = 0$, the spin is aligned along the z-axis. In a rotating frame aligned with B_1 the effective magnetic field is

$$B_{eff}(t) = B_1\hat{i} + \left(B_0(t) - \frac{\omega}{\gamma}\right)\hat{k}. \tag{3.24}$$

This process is most easily demonstrated graphically, as is done in Figure 3.4. Suppose that at $t = 0$,

$$B_0(t=0) >> \frac{\omega_1}{\gamma}, B_1 \tag{3.25}$$

so that initially the spin is essentially aligned with $\vec{B}_{eff}$. Suppose now that $B_0(t)$ *slowly* decreases in time, eventually sweeping through resonance ($B_0(t) = \frac{\omega}{\gamma}$) where $\vec{B}_{eff} = B_1\hat{i}$. $B_0(t)$ continues to decrease, until it is less than $\frac{\omega}{\gamma}$ so that, for long times t_∞, $\left|B_0(t_\infty) - \frac{\omega}{\gamma}\right| >> B_1$ and the effective field $\vec{B}_{eff}$ is essentially oriented along the $-z$ axis .

As long as the condition for adiabaticity (Eq. 3.23) is met in the rotating frame the magnetization vector will maintain alignment with $\vec{B}_{eff}$ during the entire passage, allowing for a spin flip. Thus $\frac{dB_0}{dt} << \gamma B_1^2$. A lower limit on $\frac{dB_0(t)}{dt}$ is provided by the relaxation times T_1 and T_2 in the Bloch equations. Spin reversal must occur before the polarization of the sample is lost to relaxation, requiring that

$$\frac{B_1}{T_1}, \frac{B_1}{T_2} << \frac{dB_0}{dt}. \tag{3.26}$$

Equations 3.22 and 3.26 are combined to give

$$\frac{B_1}{T_1}, \frac{B_1}{T_2} << \frac{dB_0}{dt} << \gamma B_1^2. \tag{3.27}$$

At the University of Winnipeg typical values for proton AFP are

$$4\ \frac{\mu\mathrm{T}}{\mathrm{s}} << 18\ \frac{\mu\mathrm{T}}{\mathrm{s}} << 31\ \frac{\mu\mathrm{T}}{\mathrm{s}}. \tag{3.28}$$

3.3 Experimental Method and Signal Detection

In our experiment we used a linearly polarized B_1 field, $\vec{B}_1 = B_1 \cos\omega t\ \hat{i}$ in the lab (nonrotating) frame. The net magnetic field, in the rotating frame is

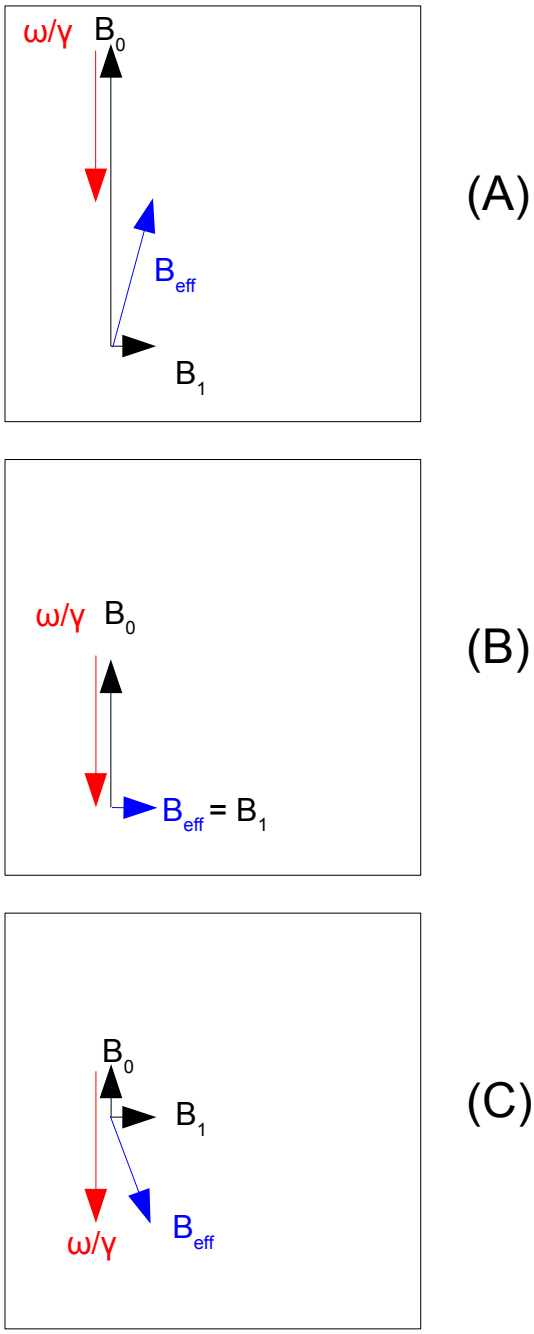

Figure 3.4: Adiabatic fast passage. (A) Effective field begins far from resonance, $\omega << \omega_0$. At this point, $\left(B_0 - \frac{\omega}{\gamma}\right) >> B_1$ and the effective field is nearly aligned with the z-axis. (B) B_0 is slowly decreased through resonance at $\omega = \omega_0$. Here, the effective field is $\vec{B}_{eff} = B_1\hat{i}$, because $\left(B_0 - \frac{\omega}{\gamma}\right) = 0$. (C) B_0 continues to decrease until $\vec{B}_{eff}$ is far from resonance and once again nearly aligned to the negative z-axis.

$$\vec{B}_{eff}(t) = \left(\frac{B_1}{2}, 0, B_0(t) - \frac{\omega}{\gamma}\right), \tag{3.29}$$

where the magnitude of the B_1 field has been reduced by half since the linear field decomposes into two equal rotating/counter-rotating fields and only one of these components is assumed to be near resonance with the nuclei.

The pickup coil placed along the y-axis of the lab frame senses an electromotive force ϵ induced by the time-varying magnetization in the y direction:

$$\epsilon = -\frac{d\Psi}{dt} \propto \frac{dM_y}{dt}. \tag{3.30}$$

The amplitude of the signal will therefore be proportional to the horizontal component of the spin and will oscillate with frequency ω. Assuming an ideal AFP case (without relaxation), the spin remains aligned with the effective field, and the amplitude $|\epsilon|$ of the signal received in the pickup coil is proportional to

$$|\epsilon| \propto \frac{B^x_{eff}}{|B_{eff}|} = \frac{\frac{B_1}{2}}{\sqrt{\left(\frac{B_1}{2}\right)^2 + \left(B_0(t) - \frac{\omega}{\gamma}\right)^2}}. \tag{3.31}$$

This shape dictates the experimental dependence of signal on ω that is observed.

3.4 Detailed Experimental Setup

Before each component is discussed, the experimental AFP NMR setup is outlined. A schematic diagram is shown in Fig. 3.5. In our setup the B_0 field is aligned along the z-axis and the B_1 field is aligned along the x-axis. A pickup coil is placed along the y-axis to detect the signal. The signal requires signal amplification, which is done using a pre-amplifier and a lock-in amplifier with phase sensitive detection. After amplification the signal is recorded using an oscilloscope for analysis.

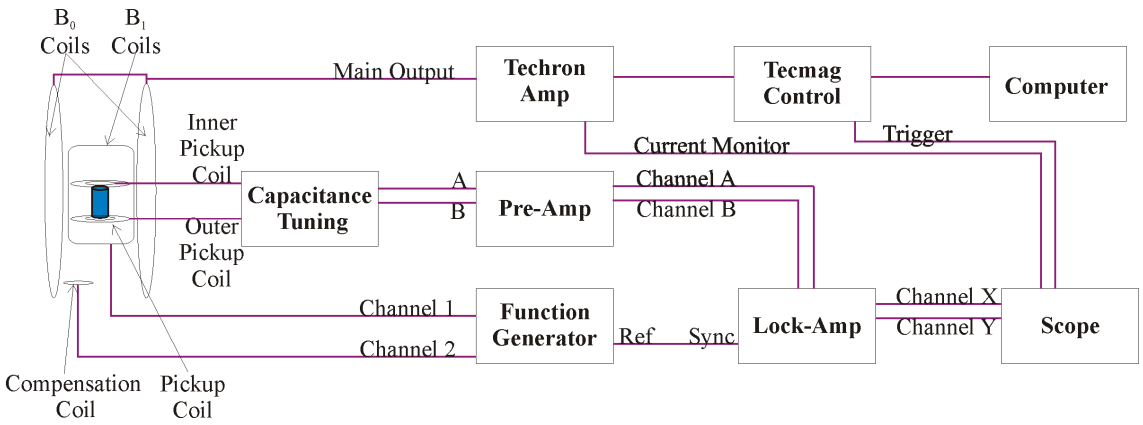

Figure 3.5: Schematic diagram of the AFP NMR setup. The coil setup is on the left and details are presented in the text. The two signals from the pickup coil enter the capacitance tuning box used to tune the system to the NMR frequency. The box outputs two separate signals A and B, the difference representing the voltage drop across a capacitor in series with the pickup coil as shown in Fig. 3.11. These signals are fed to a pre-amp and then into a lock-in amplifier. The signals are subtracted and phase sensitive detection is performed with the reference signal out from the function generator. The function generator also drives the B_1 coil (Channel 1) and compensation coil (Channel 2) at the same frequency. A computer controls the Techron Amplifier via Tecmag Control Panel, which in turn drive the B_0 coils. The x and y signals from the lock-in is displayed on an oscilloscope along with a B_0 current monitor from the Techron amplifier. Data is recorded using the oscilloscope.

3.4.1 B_0 Coil

The B_0 coil consists of planar coils (diameter $d = 52.5$ cm, $\chi = B/I = 45$ μT/A) 13 cm apart to produce a B_0 field. The coils are, in fact, the B_0 shim coil of a 3-axis planar gradient coil, originally designed for low field MRI. The coil has a maximum field strength of ≈ 10 times earth field. The B_0 coil current is controlled by an amplifier system consisting of a Techron amplifier (AE Techron 7548), Telmag consoles (Apollo Telmag control system) and a computer using NTNMR software (available from `tecmag.com`). The current is controlled in such a way that $B_0(t)$ adheres to the requirements of AFP outlined in Section 3.2.2 by slowly sweeping the B_0 field through resonance.

3.4.2 B_1 Coil

A plastic pipe (11.5 cm outside diameter, $\chi = B/I = 60$ μT/A) was patterned with copper tape to produce the B_1 field. The tape is wrapped in a saddle coil configuration, with four nested saddles on each side of the pipe, based on the design in Ref. [49]. The coil was built by Michael Lang at

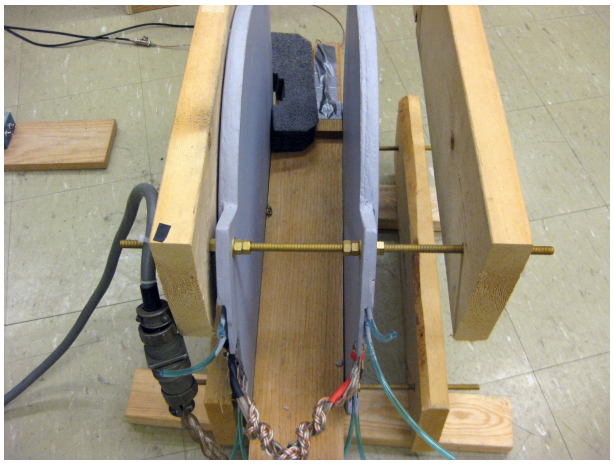

Figure 3.6: The B_0 coil used in AFP NMR. The coils are covered in grey paint.

the University of Winnipeg. This produces a uniform oscillating magnetic field transverse to the axis of the pipe. The B_1 coil magnitude is controlled by a function generator.

3.4.3 Pickup Coil

The pickup coil (shown in Fig. 3.8) is a set of two solenoidal coils of different radii. The coils are counter-wound so that the flux from external fields is nullified. This is done to reduce noise, resulting in an overall increase in signal–to–noise ratio (SNR).

To understand how this works, consider an external magnetic field B_{ext} in a general direction across the pickup coil as shown in Fig. 3.9. Both the inner and outer coils will have some flux passing through them. The coils are counterwound with, $N_{\text{inner}}A_{\text{inner}} = -N_{\text{outer}}A_{\text{outer}}$ where N is the number of turns in the coil and A is the area of the coil. Thus, any flux from a uniform external magnetic field cancels. The signal from the sample in the inner volume of the pickup coil is not nullified however, as the inner coil is more sensitve to the flux from the sample than the outer coil.

The coil is designed to be mechanically stable with a high signal to noise ratio. The pickup coil was designed and tested in our laboratory with construction and further details explained in Ref. [50].

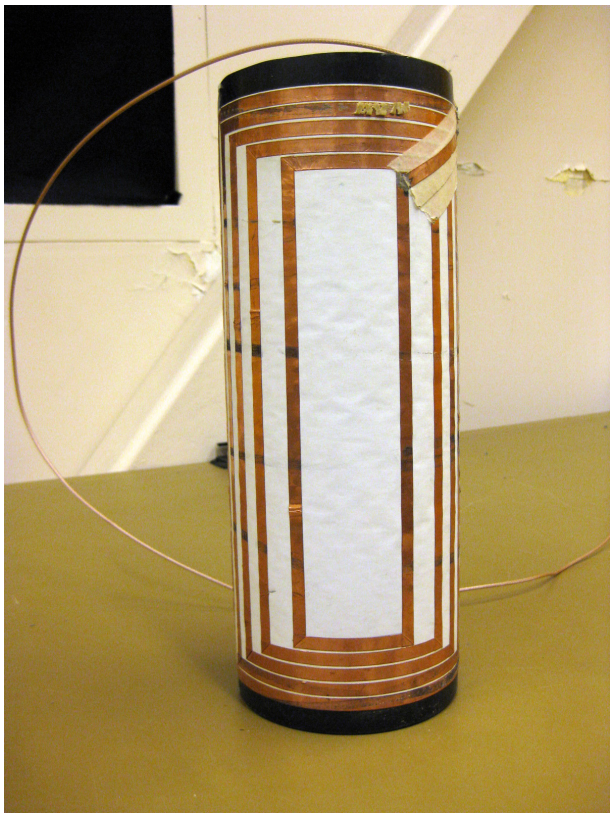

Figure 3.7: The B_1 coil used in AFP NMR.

3.4.4 NMR Signal Isolation

All three (B_0, B_1 and pick-up) coils are arranged around the experimental volume as shown in Fig 3.10. The B_1 coil is located within the volume of the B_0 coil, such that the isocenters of the two coils align. The pick-up coil is placed symmetrically inside the B_1 coil. Define the z-axis to be along the B_0 field (following convention). The x-axis and y-axis are then defined in a standard right-handed coordinate system. In this case, the x-axis is aligned to the B_1 field and the y-axis is aligned through the solenoids of the pick-up coil. Ideally the three axes will be perfectly perpendicular, but there is always some misalignment with the experimental components. This is particularly problematic with the B_1 and pick-up coils as misalignment leads to direct coupling (crosstalk) of the coils giving an unwanted signal at the target frequency that can dominate the desired NMR signal. To reduce the crosstalk between B_1 and the pick-up coils an optimal orientation is found. Any residual crosstalk is eliminated using a small compensation coil placed near the B_1 coil to induce an equal but opposite

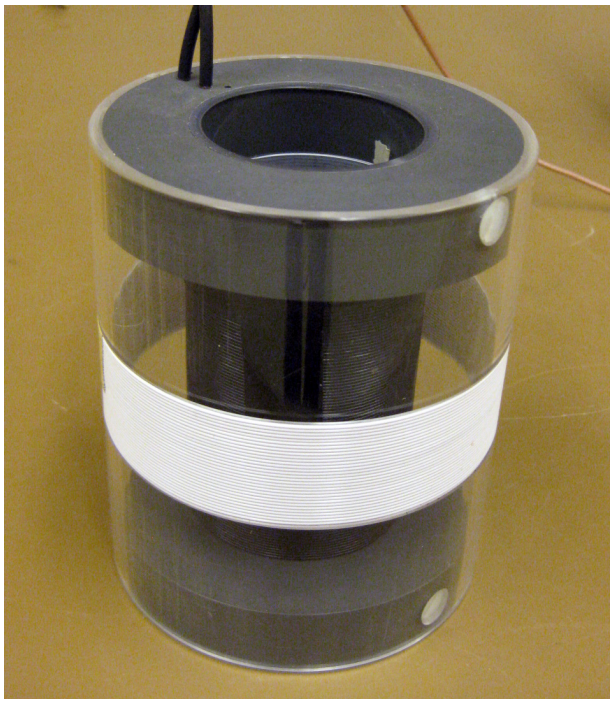

Figure 3.8: The pickup coil used in AFP NMR. The inner solenoid is black and extends the full length of the coil. The outer solenoid is white and covers the central third of the coil. The experimental sample is placed in the centre. This space is designed to accomodate a standard 125 mL Nalgene bottle.

voltage in the pick-up coils. Consider the signal voltages,

$$V_{tot} = V_{crosstalk} + V_{NMR} + V_{comp}, \tag{3.32}$$

where the signal in the lock-in amplifier V_{tot} is the total signal received from the pickup coil, $V_{\text{crosstalk}}$ is the unwanted signal arising from crosstalk, V_{NMR} is the desired NMR signal, and V_{comp} is the signal generated by the compensation coil. By setting the compensation signal such that $V_{\text{comp}} = -V_{\text{crosstalk}}$ resulting in V_{tot} being only the desired V_{NMR}.

The phase and amplitude of V_{comp} is adjusted on the function generator controlling the compensation coil. The process to eliminate crosstalk is as follows. Measure both the amplitude and phase of the signal on the lock-in amplifier with the compensation coil turned off and the B_1 coil turned on. Once the signal is noted, the B_1 coil is turned off and the compensation coil is turned on. The amplitude and phase of the compensation coil are adjusted so that the same signal amplitude registers on the lock-in amplifier. The phase is then set to be 180° out of phase with the signal

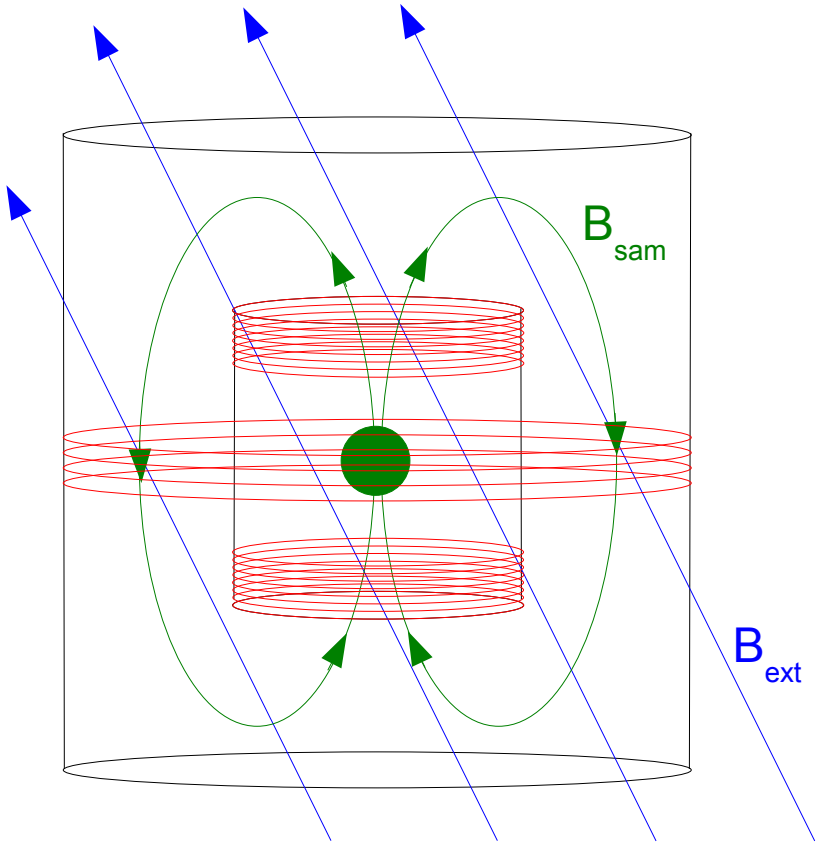

Figure 3.9: Pickup coil sensitivity to external and internal fields. An external field (blue) produces an equal flux through both the inner and outer coils (red), which can cancelled by counterwinding. The inner coil is more sensitve to an internal dipole (green) since the flux lines pass through it in only one direction. The outer coil will receive no signal from the same pair of flux lines. Using this pickup coil therefore results in decreased sensitivity to external sources. The number of windings shown has been reduced from the actual number of windings for clarity.

noted with just the B_1 coil on. Both coils are then turned on and a signal close to zero is recorded on the lock-in amplifier. Usually this is done with B_0 turned off. Turning B_0 on makes a small impact on the signal due to additional noise, but it can be negated by electronically re-zeroing the lock-in amplifier.

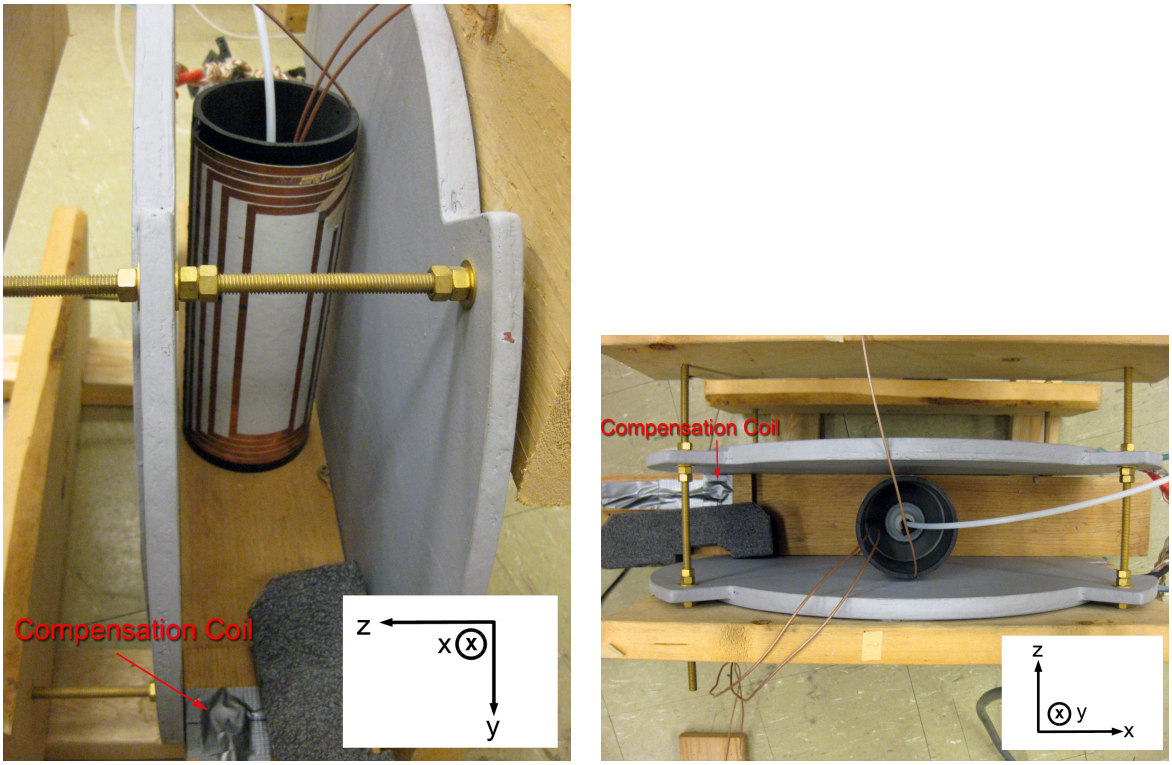

(A) (B)

Figure 3.10: Coil arangement used in AFP NMR. (A) side view showing the orientation of the B_1 coil within the B_0 coil. (B) top view showing the pickup coil inside the B_1 coil. The small coil on the plank of wood wrapped in tape is the compensation coil. It is located at the bottom of (A) and on the left side in (B).

3.4.5 Phase Sensitive Detection

The AFP-NMR signal is small (∼nV). To sense and amplify the signal, the two pick-up coils are connected in series and tuned to the resonant frequency ω_0 with a parallel capacitor (see figure 3.11). The resulting RLC resonant circuit serves two purposes. Firstly, it increases the signal strength by the quality factor Q of the circuit. Secondly, it increases the resistance to the pre-amplifier by $\sim Q^2$ to better match the noise figure of the pre-amplifier, helping to maintain the intrinsic SNR of the

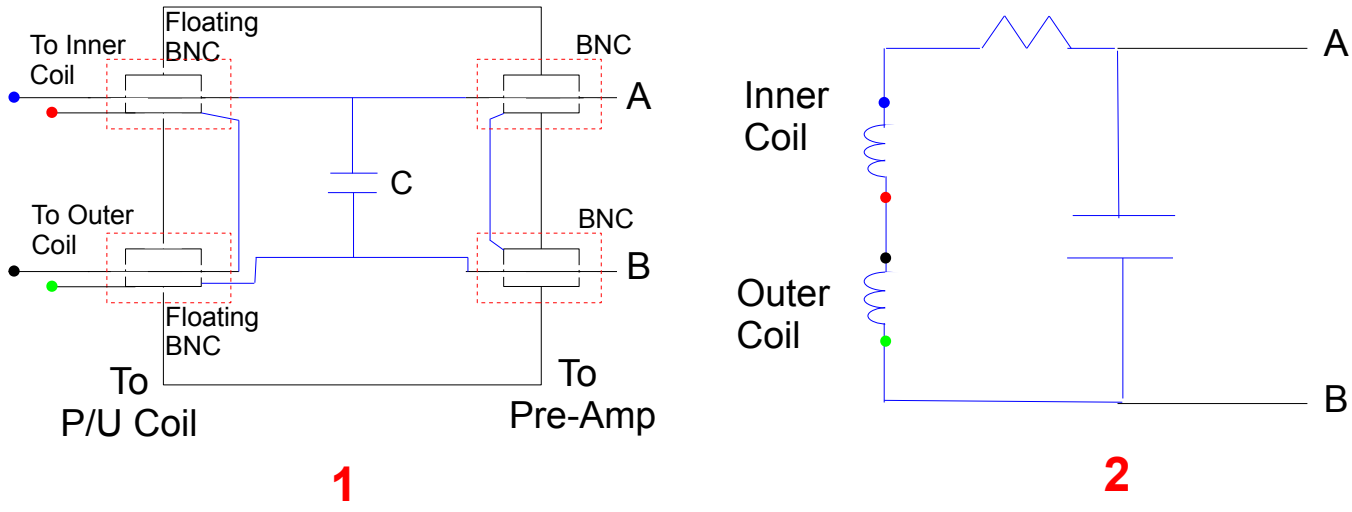

Figure 3.11: (1) Schematic diagram of capacitor tuning box. Two BNC connectors are on each side of the box. On the pick-up coil side, the BNC cables are constructed such that the central conductor is one lead of the coil and the floating coaxial shield is the other lead. On the pre-amp side, signals A and B are output along the signal wire of the BNC. (2) Functional diagram. The tuning box adds the two pickup coils together in series and then places a capacitor across the combination, resulting in the circuit shown. The coloured circles are added as reference points relating the two diagrams together. The resistance shown is the combined resistance of the pickup coils and tuning box.

pick-up coils.

A different capacitor is used to match the ω_0 of the different nuclear species used here (protons and Xe-129). For water NMR at 25.8 kHz, a 37 nF capacitor was used. For Xe-129 NMR at 7.2 kHz a 502 nF capacitor was used. Both frequencies are set by the gyromagnetic ratio of the nucleus being used and the selected strength of B_0. Ultimately, the maximum field strength of B_0 was set by the maximum current that could be applied to the B_0 coil.

The voltage across the capacitor is then passed to a pre-amplifier. The output of the pre-amplifier is then sent to a lock-in amplifier (SR830 DSP) operated in differential (A-B) mode. The reference frequency is set to be equal to the oscillation frequency of the B_1 field using the trigger output of the variable amplitude function generator (Agilent 33522A) which drives the B_1 coil. The X and Y outputs of the lock-in amplifier are viewed using a digital storage oscilloscope (TDS2004B) equipped with a USB port for data storage.

Chapter 4

Results

4.1 Laser Characterization

A detailed understanding of the laser performance is important for optimizing the SEOP process. In particular, the laser wavelength needs to be tuned to the D1 absorption line of rubidium. Because the D1 line is extremely narrow ($\lesssim$ 10 GHz) relative to the laser full-width half-maximum ($\sim$ 150 GHz), pressure broadening (to $\gtrsim$ 200 GHz) is used to maximize absorption. For our laser, the temperature of the laser base is used to tune the laser wavelength to maximize absorption.

There are three different temperatures involved in laser operation. The first is the temperature of the chiller plate, the second is the temperature of the laser base, and the third is the actual diode temperature. The chiller plate temperature is externally set and regulated by the cold water supply pump. The laser base temperature is measured by a thermistor built into the laser housing. The laser diode temperature itself cannot be measured, directly, but is the quantity most directly related to laser wavelength. The laser base temperature rises dependent on the laser current selected. The larger the laser current, the larger the laser diode and base temperature difference relative to the chiller plate temperature. The difficulty encountered in tuning the laser and controlling its output power is therefore to simultaneously set the chiller temperature and laser current to achieve long term stable operation. Since the laser's base temperature is the temperature most closely related to the actual diode temperature, we also recorded this temperature in these studies.

In further communication with the laser manufacturer, we learned that the laser wavelength itself is the best monitor of the actual diode temperature. Therefore, instead of observing the recommended cutoffs on the laser base temperature as a means to prevent accidental over temperature of the laser diode, we eventually decided that as long as the laser wavelength was below 795.56 nm, the diode would be operated safely. In addition, the laser power supply is set to turn off if the laser base temperature exceeds a certain value. The factory setting of this value was 30 °C. We found that for lower laser output power, we were continually approaching this cut off value when setting the laser temperature high enough to reach 795.56 nm in laser wavelength. We therefore raised the trip point in the laser's base temperature to 35 °C, and carefully monitored the laser wavelength not to exceed 795.56 nm when deciding to tune to higher wavelengths at lower laser power. In practice, the chiller plate itself provided a constraint on the maximum operating temperature as it was unable to warm up past 30.4 °C.

Our laser was designed to have a wavelength of 795.00 nm at a current setting of 38.0 A and base temperature of 18 °C requiring a chiller temperature of 13 °C. However, we did not want to run at such a high current (and therefore laser power) in all situations, so the relationship between base temperature and laser wavelength was carefully characterized. The setup to achieve this was as follows. The laser beam was collimated into a one inch beam directly after the fibre output. The majority of the beam was directed into a power meter (Newport Hand-held Optical Meter Model 1918-C) used simultaneously as a beam dump. A small percentage of the beam was diverted into a spectrometer (Ocean Optics Jaz) using a glass microscope slide. The laser was set to a fixed current and the chiller plate temperature is set. The laser's base temperature and the central wavelength (as indicated by the spectrometer's software) was recorded. The chiller plate temperature was then increased until either the laser wavelength was too high (over 795.56 nm) or the maximum temperature for the chiller plate was reached ($\approx$ 30.4 °C). Laser power was also recorded for each trial.

Figure 4.1 shows the measurements of laser's base temperature and the wavelength sensed on the spectrometer when various chiller plate temperatures and laser currents were set. The data was taken by setting the chiller plate temperature to a particular value and allowing the temperature of

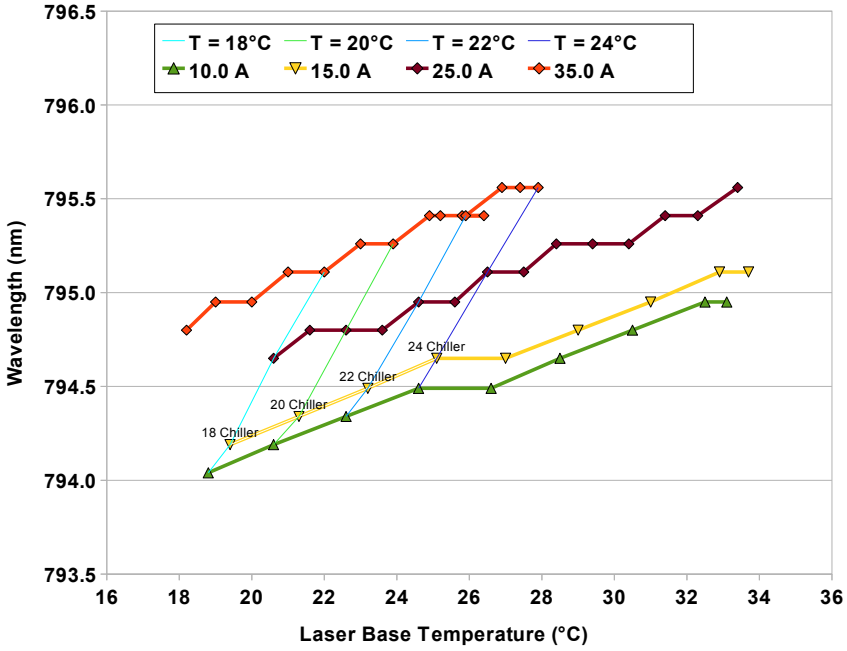

Figure 4.1: Laser current and chiller plate temperature profiles for selecting laser wavelength and the laser's base temperature. The legend lists the four laser diode currents used in the measurement, indicated by the thick lines on the graph. Also listed in the legend are four of the multiple set temperatures for the chiller plate that were used in the measurement. The measured wavelengths and measured temperature of the laser base for the set chiller plate temperature and diode current are annotated with the chiller lines. These thin lines can be used as a quick quide for setting the chiller plate temperature to achieve a desired laser wavelength. The unlabelled data points are for 1 °C increments on the chiller set temperature. The laser power is proportional to the laser current, which is shown in Fig 4.2 and the associated discussion in the text.

the laser base to equilibrate. The laser current was then set to a particular value and the temperature and laser wavelength was allowed to again equilibrate. Holding the laser current constant, the chiller plate temperature was increased in 1 °C increments. After each increment, the laser wavelength and temperature of the laser base were both allowed to equilibrate. The time to reach stable values in the laser wavelength and temperature of the laser base was typically 5 minutes. At this time, the laser wavelength and the temperature of the laser base would be recorded. The temperature of the chiller plate would then again be incremented by 1 °C. The temperature of the chiller plate was increased in this fashion until either the maximum value was reached (30.4 °C) for the chiller plate, or the central wavelength obtained at that specific chiller plate temperature was deemed too high (over 795.56 nm). The whole process was repeated for four different laser current settings: 10.0 A, 15.0 A, 25.0 A and 35.0 A.

The data in Fig. 4.1 indicates that as the chiller plate temperature is increased, both the temperature of the laser base and the wavelength increase, as would be expected. What is interesting and important in Fig. 4.1 is the trend of these values with different laser currents. For higher laser currents, longer wavelengths can be reached with modest chiller plate and corresponding laser base temperatures. Whereas, for lower laser currents the chiller must be set to rather high temperatures. Evidently the true laser diode temperature is larger than 34 °C when the laser is in operation at 795.00 nm. It is laser wavelength that is therefore the best monitor of the true diode temperature and the safety of the laser.

Figure 4.2 reports the corresponding measurements of the laser power, measured simultaneously with the results displayed in Fig. 4.1. The points in Fig. 4.2 therefore report controlled 1 °C increments of the chiller temperature. As expected, the laser power increased linearly with the laser current, once a specific minimum laser current I_{th} has been reached. This current is known as the threshold current. Somewhat unexpected was a slight decrease in laser power as the temperature was increased.

This may be understood qualitatively in terms of the characteristic temperature of the laser diode. As the temperature T of the laser diode increases, the threshold current $I_{th}(T)$ to achieving lasing increases exponentially as $I_{th}(T) = I_0 e^{T/T_0}$ [51] where I_0 is a constant and T_0 is the charac-

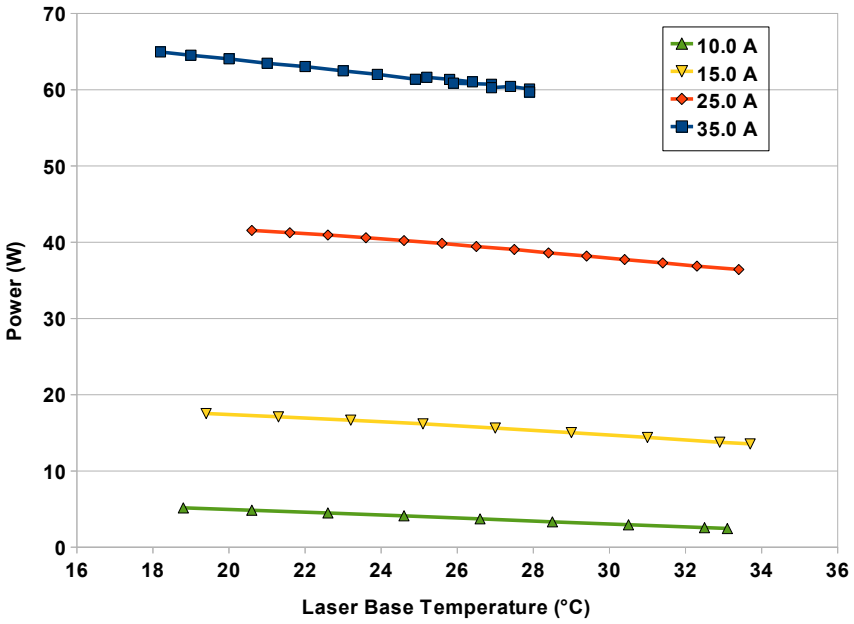

Figure 4.2: Laser power loss with increasing temperature at different diode current values. After investigation, the power loss is due a well known trait of diode lasers, that the threshold current increases with increasing T, lowering the power output at higher temperatures.

teristic temperature. Typically, I_{th} increases of order a percent per degree Celsius for diode lasers. Therefore, as the diode temperature increases for a fixed laser current, the laser output power will drop.

4.1.1 Polarization

The laser polarization is linear coming out of the laser diode. However, the polarization apparently degrades after travelling through the optical fibre coupling. The net laser power available for SEOP can be determined by measuring the linear polarization of the beam. This is done by passing the beam through a polarizing beam splitter cube into a power meter (Newport Hand-held Optical Meter Model 1918-C) and analyzing the relative power of each polarization component. Polarization may be calculated using

$$P = \frac{S_{\rightarrow}}{S_{\uparrow} + S_{\rightarrow}}, \tag{4.1}$$

where $S_{\rightarrow}$ is the signal from the horizontally polarized beam (main beamline) and $S_{\uparrow}$ is the signal from the vertically polarized beam (secondary beamline). The orientation of the two polarized components was found using a linear polarizer placed after the polarizing beam splitter. Our setup transmits 89% of the laser power along the main beamline resulting in a polarization loss due to the optical fibre of 11%.

4.2 Proton AFP

4.2.1 Water Calibration

The AFP-NMR system was tested using a 125 ml plastic bottle of water. The actual volume of water was 147 ml because it was filled to the cap. The bottle itself is the same as the bottle used as a gas sample volume in the flow through system for xenon. Water NMR provides a way to calibrate the Xe polarization since the water polarization is known according to the Boltzmann polarization, as discussed in Section 4.4.

The largest challenge in using water is that the polarization is small. The protons in the water are thermally polarized. The energy level difference between the spin up and spin down states is given by the strength of the B_0 field. The low magnetic field that we used produced a small energy difference, leading to a polarization $\sim 2 \times 10^{-9}$ (the calculation of the polarization is discussed in Section 4.4). To compensate for the weak signal from water multiple trials would generally be taken in succession and averaged.

Figure 4.3 displays an AFP-NMR result for water. Two resonances are observed in the signal: one at the resonance point when the B_0 field passes through resonance sweeping up and the second at the resonance point ramping down. In between the two peaks the proton spin relaxes back to equilibrium because the T_1 relaxation time ($\approx$ 1 s) is shorter than the sweep time ($\approx$ 5 s). The second peak therefore appears as a valley, or phase shifted by 180° relative to the first resonance peak.

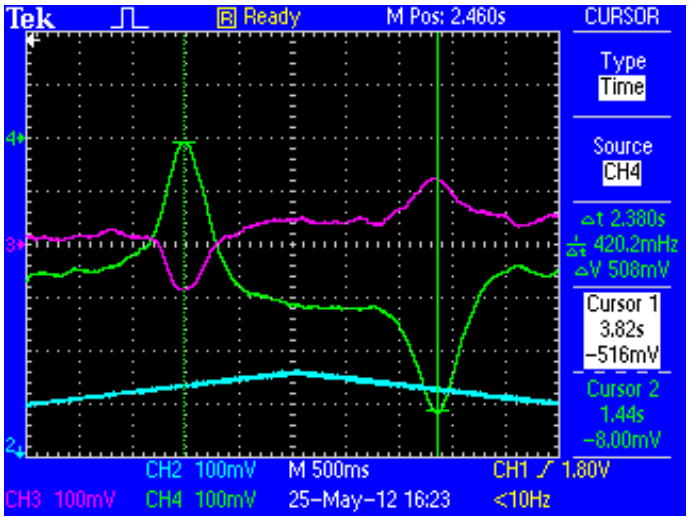

Figure 4.3: Averaged oscilloscope trace showing AFP signals from water taken over 16 averages. Blue is the B_0 ramp (current monitor), green is the y channel of the lock-in amplifier and pink is the x channel of the lock-in amplifier. Resonance points are marked by the green vertical lines. The first peak/valley is on the upward pass through resonance. The second valley/peak is on the downward pass through resonance. The signal has reversed direction since the spins relaxed back to the initial conditions in between resonance points. The total time displayed is 5 s. The signal is split between the x and y channels due to an arbitrary phase shift of the B_1 field relative to the lock-in amplifier phase.

4.2.2 Noise Characterization

The signal being detected is small enough that noise present in the electronics can override and wash out any signal that may be present. Tests were therefore conducted to characterize the noise.

Beginning with only a pre-amplifier, lock-in amplifier, and oscilloscope, the noise was characterized. Other electronics were systematically added and the impact on noise was observed. Table 4.1 shows the experimental parameters for each piece of equipment in use. Figure 4.4 shows the progression of noise as equipment is added. Table 4.2 shows the configuration for each trial and summarizes the results, which we now discuss.

Equipment	Settings
SR552 Bipolar Preamplifier	A-B setting
SR830 DSP Lock-in Amplifier	Time constant: 100 ms, 12 dB. Sensitivity: 500 μV. Signal: A-B, DC, Float. Reserve: normal. Channel One: X, oscilloscope channel 3. Channel Two: Y, oscilloscope channel 4. Reference Frequency: 25.8 kHz. Reference Amplitude: 0.300 V. Reference Phase: 0° Reference Trigger: Internal trigger or trigger from waveform generator.
Tektronix TDS 2004B Oscilloscope	X: 500 ms major scale division, 5 s total view. Y: Channel 1 and 2: Unused. Channel 3: 50 ms major division. Channel 4: 50 ms major division. Scan mode.
Agilent 33522A Waveform Generator	Channel One: Frequency: 25.8 kHz, Amplitude: 1.4 Vrms, Offset: 0 V, Phase: 0°. Trigger: out to lock-in amplifier. Channel Two: Frequency: 25.8 kHz Coupled, Amplitude: 6.338 Vpp, Offset: 0 V, Phase: 271.99°.

Table 4.1: Experimental settings of electronic equipment used for signal analysis.

Trial 1 consisted of the pickup coil signal, the pre-amplifier, and the lock-in amplifier. The lock-in amplifier sensitivity was set at the same level typically used during AFP trials. The B_0 and B_1 fields were both off, as was the waveform generator used to drive the B_1 coil. Usually the waveform generator sends a trigger to the lock-in amplifier, but this was disabled and the internal trigger of the lock-in amplifier was used for Trial 1 instead. For Trial 2, the waveform generator was turned on, but not driving B_1, and the lock-in amplifier trigger was switched back to external. For Trials 3 and 4, all the control equipment for the B_0 coil was switched on, including the amplifier.

The amplifier was not enabled until Trial 5, and even then had no current flowing through it (i.e. B_0 was still null).

Based on this data it was concluded that the Techron amplifier contributed a nearly three-fold increase in noise when it was enabled. The other equipment contributed a negligible amount of noise compared to the minimum noise present in trial 1.

Trial	Equipment On	Result
1	Pre-amp, Lock-in amp (internal trigger), Oscilloscope	$\Delta V = 58$ mV
2	1 plus Waveform Generator, Lock-in amp (external trigger)	$\Delta V = 58$ mV
3	2 plus Tecmag boxes and Computer	$\Delta V = 62$ mV
4	3 plus Techron Amplifier in standby	$\Delta V = 60$ mV
5	3 plus Techron Amplifier enabled, no current flow	$\Delta V = 162$ mV

Table 4.2: Noise levels arising from acquisition electronics. The result ΔV reports the max-min noise level observed in Fig. 4.4.

4.2.3 Amplifier Ramp Tests

The current for the B_0 field was supplied by a Techron amplifier controlled by a Windows PC running NTNMR software via Tecmag control electronics. The amplifier output was controlled in the software by specifying the desired percentage of a set maximum output level. In order to create a current ramp, and by extension a B_0 ramp, small discrete steps must be specified. A sample oscilloscope trace displaying various step sizes is presented in Fig. 4.5. As is obvious from Fig. 4.5, care must be taken to ensure the adiabatic condition on the maximum B_0 sweep rate is satisfied (Equation 3.23) at the edges of the steps. This effect was studied using the B_0 sweep sequence depicted in Fig. 4.6, where, during the ramp times (indicated by region 3 in Fig. 4.6), various numbers of steps were used.

The ramp goes from 89.5% to 99.5% of the maximum set level in 2.5 seconds and then back down to 89.5% in the next 2.5 seconds. Ramps of 10, 100, 200, 1000, 2000, 5000 and 10000 steps, (corresponding to step sizes of 250 ms, 25 ms, 12.5 ms, 2.5 ms, 1.25 ms, 0.5 ms and 0.25 ms respectively), were tested. All results are taken as a 16 trial average on a water sample.

The Y channel output of the lock-in amplifier for each trial is plotted in Figure 4.7. A step size

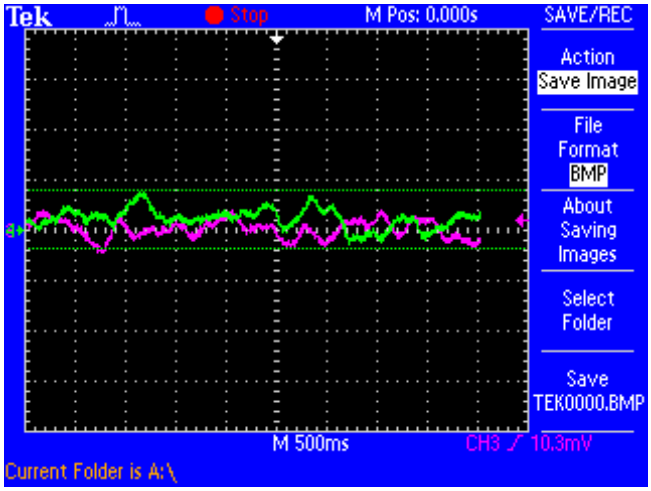

Trial 1

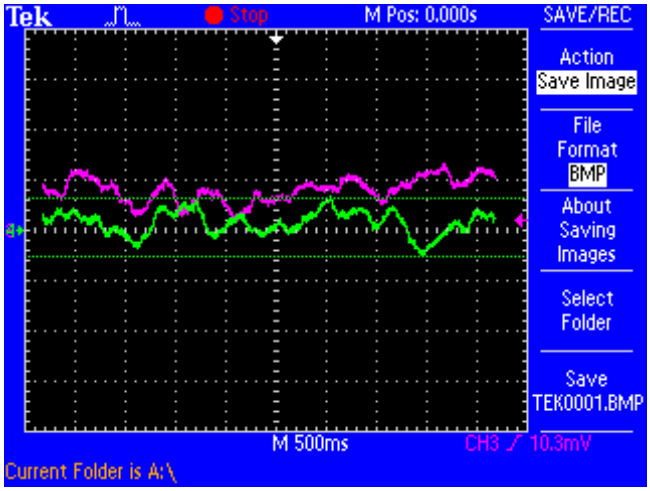

Trial 2

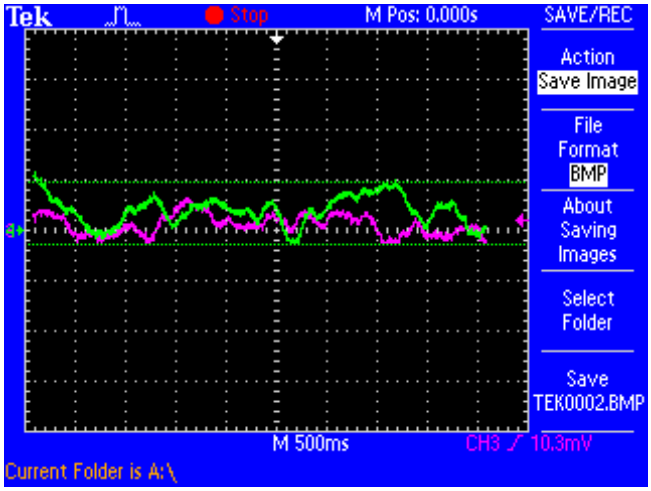

Trial 3

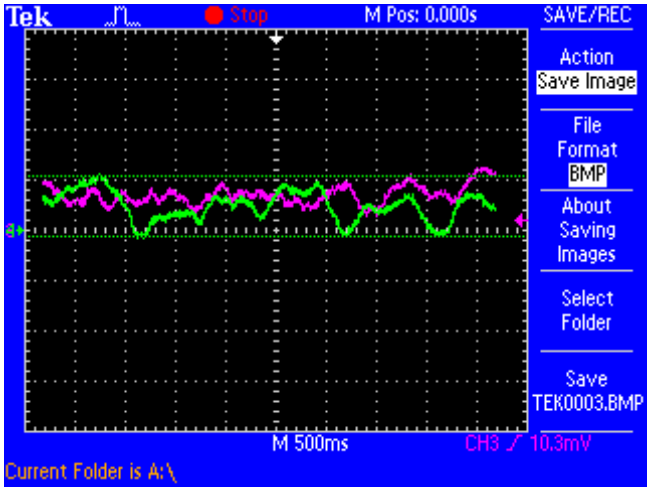

Trial 4

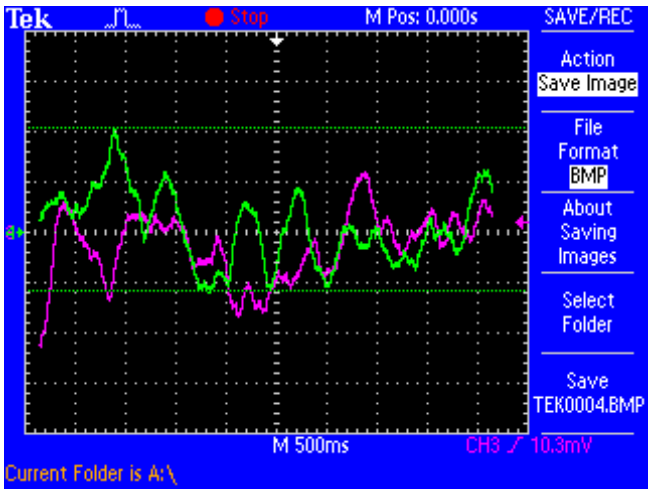

Trial 5

Figure 4.4: Oscilloscope outputs from each of the 5 background trials described in Table 4.2 for determining baseline noise.

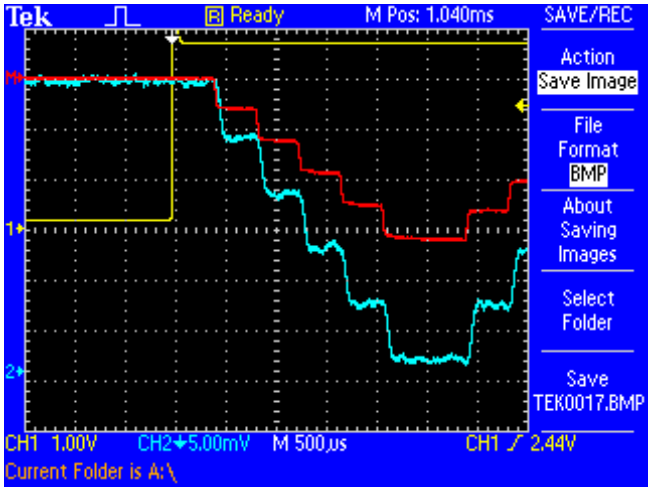

(A)

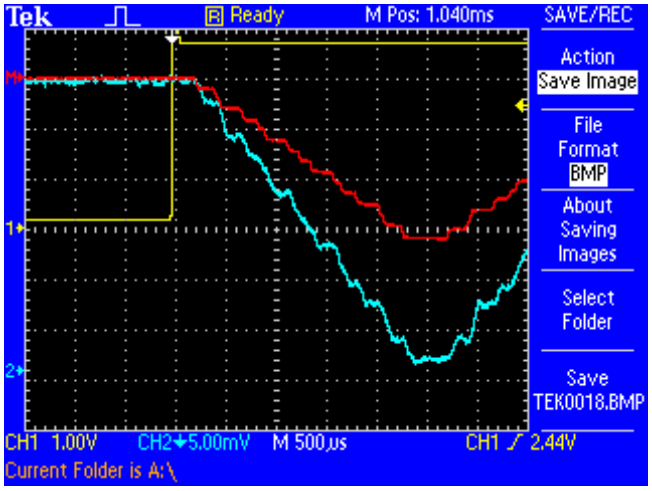

(B)

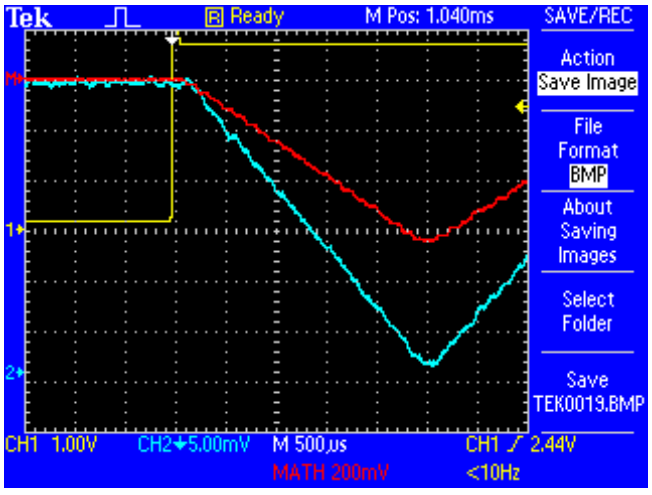

(C)

Figure 4.5: Oscilloscope outputs from a (A) 5 step ramp, (B) 10 step ramp and (C) 20 step ramp. More steps over the same time period represents a smaller step size. The amplifier current is red and the produced magnetic field is blue. Each horizontal division is 500 μs resulting in a total ramp time of 2.5 ms.

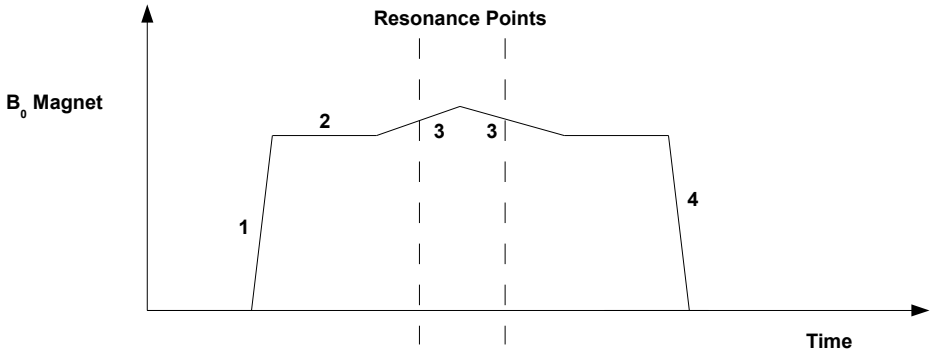

Figure 4.6: Basic AFP sequence sent to the amplifier. The ramp has four characteristic regions: 1) Quick initial ramp to just below the resonance condition; 2) Prepolarization; 3) Slow ramp through resonance in both directions; 4) Quick exit ramp.

of 250 ms is clearly insufficient, while the other trials give good signals. There is an upward trend in peak height as step size decreases across the 25 ms, 12.5 ms and 2.5 ms step sizes. This trend could be caused by an inefficient spin flip at these larger step sizes (> 2.5 ms) due to the B_0 field changing too sharply. Any step size smaller than 2.5 ms has no noticable increase in peak height. At this step size the ramp appeared visually "smooth" on the oscilloscope. Thus, there is no increase in peak height as step size decreases as the ramp can not get "smoother". The two fastest step times (0.5 ms and 0.25 ms) do not align (in time) with the peaks from the previous four trials. This was likely caused by a small change in the local magnetic field, causing the resonance point to be at a slightly later point in the ramp. This was likely caused by the last two trials being completed at a later time. The amplifier is capable of step sizes as small as 100 ns/step and therefore the finest step size of 0.25 ms (10000 steps over 2.5 seconds) was used henceforth.

4.3 Hyperpolarized Xenon

4.3.1 Sample AFP-NMR Spectra

The gyromagnetic ratio of Xe-129 is $\gamma_{\mathrm{Xe}} = -11.777$ MHz/T compared to a proton's gyromagnetic ratio of $\gamma_p = 42.576$ MHz/T. This requires that the B_1 drive frequency be set to a lower frequency (corresponding to the new Larmor frequency) and the B_0 sweep time be increased, compared to

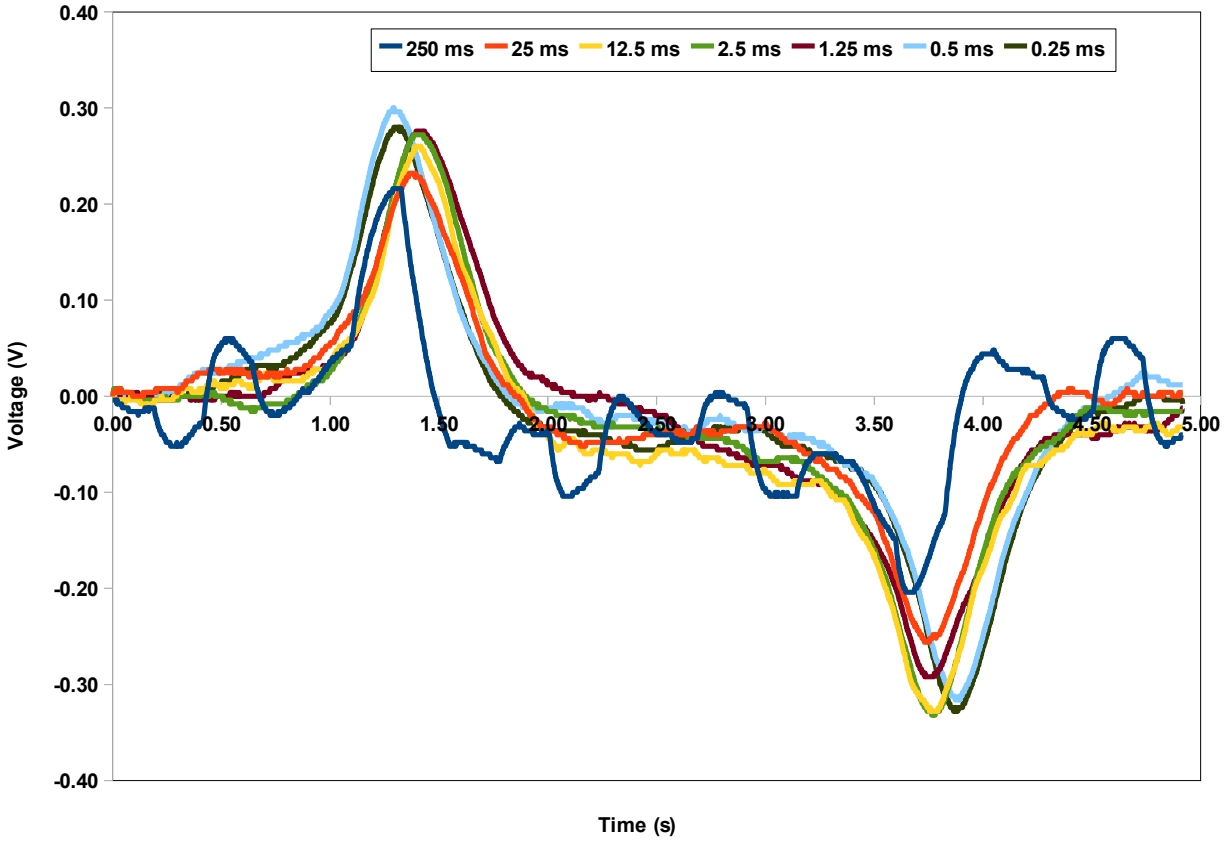

Figure 4.7: AFP NMR Y channel output of water for various step sizes, indicated by the legend. All trials are adjusted to have an equal signal at $t = 0$. The maximum signal size is obtained at a step size of 2.5 ms or smaller. The shift of the peak location in time (of the 0.5 ms and 0.25 ms step sizes) is caused by running the experiment at a later date time. A slight change in local magnetic field strength compared to the inital trials is expected to be the cause of the shift.

the sweep time used in water AFP. The constraint on the sweep time results from the inequality presented in Equation 3.27.

The increased sweep time, combined with the flow-through nature of the Xe gas delivery system made signal averaging more difficult. However, the signal to noise ratio of the Xe trials was higher than that of water which allowed for single sequence acquisitions to be made without averaging.

A sample result of AFP-NMR of hyperpolarized Xe-129 is shown in Fig. 4.8. The result shows two peaks corresponding to the signal obtained during two passes through resonance.

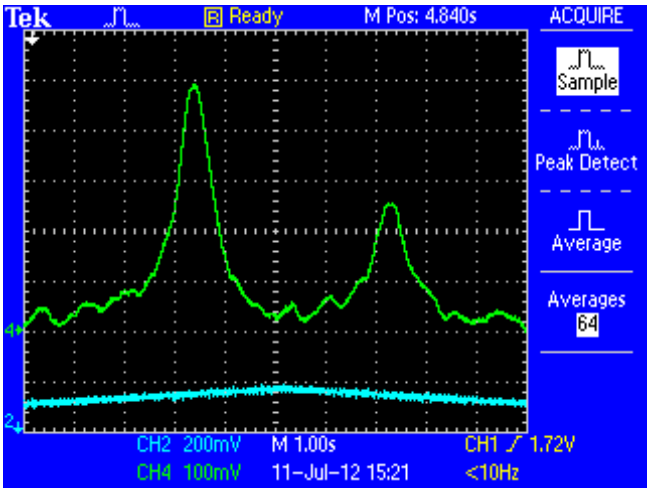

Figure 4.8: AFP-NMR result using a single sequence of hyperpolarized xenon.

The peaks can be changed to valleys set by changing direction of the magnetic field around the SEOP cell, or by switching the helicity of the laser light by rotating the quarter wave plate. Typically, experiments were performed with the first peak in the up direction. The most noticeable difference between water AFP (Fig. 4.3) and xenon AFP (Fig. 4.8) is the direction of the second peak relative to the first. This arises from the longer T_1 relaxation time of xenon, so that relatively fewer xenon atoms have relaxed to equilibrium before the down sweep. Furthermore, xenon is not Boltzmann polarized like water, so if a long time elapsed between the peaks, the second peak would disappear rather than be of opposite sign. However, as described in the next section, an opposite sign peak may be observed if the flow rate of the Xe replenishes the spins before the down sweep.

4.3.2 Continuous Flow vs. Single Fill

The flow of hyperpolarized xenon to the experimental cell is controlled by a needle valve at the exit of the polarizer. If the valve is closed before the AFP sequence starts (single fill trial), the xenon flow stops. Some xenon will leak out of the cell through holes in the cell and this is one way signal can be lost in single fill mode. Signal can also be lost by xenon in the wrong spin state diffusing into the AFP region. Wrong spin state xenon refers to the xenon that does not undergo a spin flip during the first pass through resonance. This wrong spin state xenon remains in the system in the plastic tube used for transport between the needle valve and the AFP region, which can then diffuse into the AFP region after the first pass through resonance, resulting in a lower net magnetization in the AFP region. Relaxation also causes signal to be lost. These three factors lead to the second AFP peak to be smaller than the first. A sequence of closed valve trials can be used to find the T_1 relaxation time and is discussed in Section 4.3.4. When finding the T_1 relaxation time, we assume that relaxation is the dominant source of signal loss.

If the valve is left open, the experiment is considered to be running in continuous flow mode. This means that while the AFP sequence is running, fresh hyperpolarized xenon is entering the cell. This can be used to determine how long it takes for the experimental volume to be refilled.

4.3.3 Refill time

The AFP sequence was modified to include a wait time between the up and down AFP ramps (as shown and indicated by region 5 in Fig. 4.9). After the first AFP ramp, the magnetic field is held at a high (relative to resonance) level for a set amount of time. By varying this time, and keeping the flow rate and all other parameters constant, the refill time of the experimental volume can be found using NMR. The data obtained is shown in Fig. 4.10, where for each of the panels in Fig. 4.10 a different time between the two current ramps is used. In each panel two peaks are observed. The first peak arises from the first sweep through resonance in the AFP B_0 sweep sequence. The second peak arises from the second pass.

The first peak can be seen to be of essentially the same height in all of the panels of Fig. 4.10.

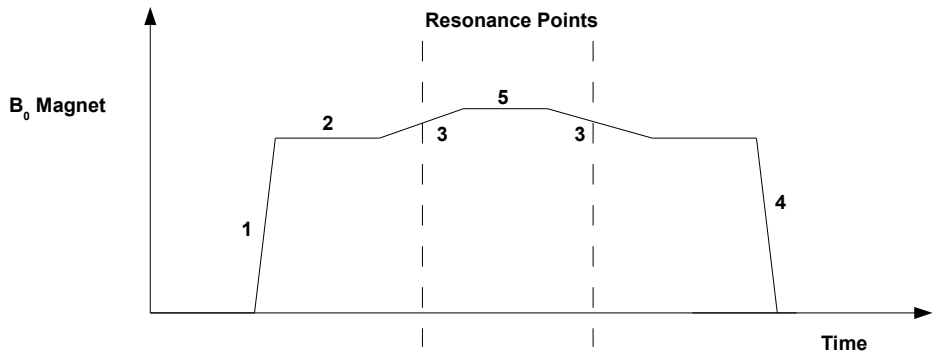

Figure 4.9: A plateau is added after the first AFP ramp to increase the time between the two resonance sweeps. This allows for the refill time of the bottle or the T_1 relaxation time to be found.

This is not surprising because all experimental parameters were the same up to this point in the sequence. The first peak is therefore indicative of the stability of the system over the trials. The second peak, on the other hand, is seen to get smaller and even reverse sign as the time between the two ramps is increased. This evolution can be understood in the following qualitative way.

Suppose the Xe spins begin in the spin "up" state. After sweeping through the first resonance point (when the magnetization of the existing xenon in the bottle is reversed to the spin "down" state), fresh xenon in the "up" state will continue to enter the bottle due to the continued flow of the Xe through the system. The freshly introduced xenon is in the opposite spin state compared to the xenon currently in the bottle. The mixture of spin up and spin down will reduce the magnetization and hence the second resonance peak's signal. The longer xenon refills the bottle between peaks, the lower the second peak will be, eventually reversing the peak into a valley. Once enough time between the peaks has elasped, all the xenon in the cell will have been refreshed back to the spin up state. The second pass through resonance will now produce a valley of the same magnitude as the original peak.

The time required for a full peak inversion should be approximately equal to the average time required to completely refill the bottle with new hyperpolarized Xe-129. The data shown in panels G and H of Fig. 4.10 show a valley that is equal in magnitude to the initial peak within the error of the measurement signified by the baseline noise visible in the panels. A refill time of 25-30 seconds is therefore suggested (the time between the two resonance points in panels G and H of Fig. 4.10).

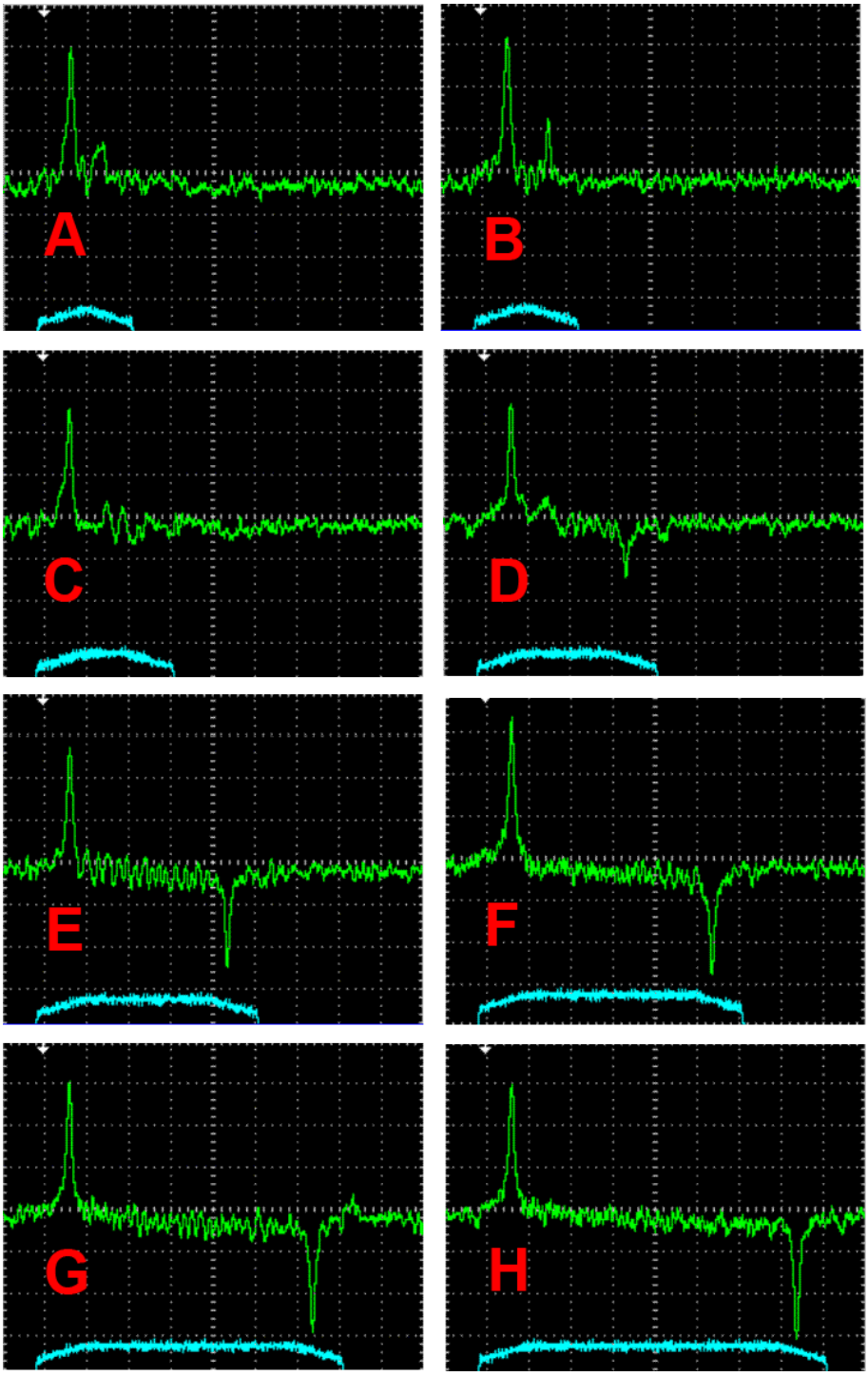

Figure 4.10: Oscilloscope traces showing xenon refilling the experimental volume over time. Oscilloscope traces are in alphabetical order with increasing time between peaks. The first trace (A) has minimal time between the two peaks. Fresh xenon is flowing into the cell over time, resulting in the second peak getting smaller then flipping negative (B - G). Trace (H) shows a second peak of the same magnitude of the first peak, indicating the entire experimental bottle has been refilled between the resonance points. The time between the peaks is therefore interpreted as the refill time. AFP sequence is shown in Fig. 4.9.

This deduction based on NMR can be compared with data based on the flow rate of the Xe gas into the measurement volume. The flow rate according to the flow meter was 0.25 slm. The flow meter was calibrated for helium. With the gas mixture being over 96% He, the flow rate measured by the flow meter was assumed to be in good agreement with the actual flow rate. The volume of the measurement bottle was 147 mL. Therefore, the refresh time for the bottle is expected to be 0.147 L/(0.25 L/m) = 35 s. The measurement based on NMR and the measurement based on flow rate are therefore qualitatively in good agreement.

4.3.4 T_1 Measurement

T_1 is measured by varying the time between two consecutive AFP ramps with the gas flow stopped prior to the first ramp. If T_1 is longer than the time between the resonance points, two peaks in the same direction will be visible as explained in Section 4.3.1. The first peak measured is used for normalization, while the second peak is used to determine T_1.

The polarizer was tested and working a set of operating parameters giving a large as possible first peak was determined prior to conducting these measurements. The procedure followed to conduct the measurements is now described. The computer software was programmed with the sequence displayed in Figure 4.9. As soon as the sequence was started, the needle valve was manually closed to stop the xenon flow. Another feature of the experimental setup during these measurements was that the bottle was purposely tightly capped and any obvious holes were sealed with tape. This was done to minimize the possible effect of leaks on the extraction of T_1, although no careful systematic study was conducted. After the ramp sequence completed, data was stored on the USB thumb drive in the oscilloscope. Hyperpolarized Xe was allowed to refill the measurement chamber for a few minutes before the next measurement. After this procedure was completed, the valve was re-opened and the bottle was refreshed with new hyperpolarized xenon. The time between ramps was then increased and the procedure repeated.

For accuracy, raw data was only used if the first peak values were within 15% of the maximum seen before starting. In this case, the minimum acceptable signal was 300 mV. If the first peak signal was too small, the trial was thrown out and the procedure repeated with the same settings.

Errors of this sort were possible due to the manual closing of the needle valve, which was not timed precisely (although care was taken to close it in the same fashion as much as possible over the trials).

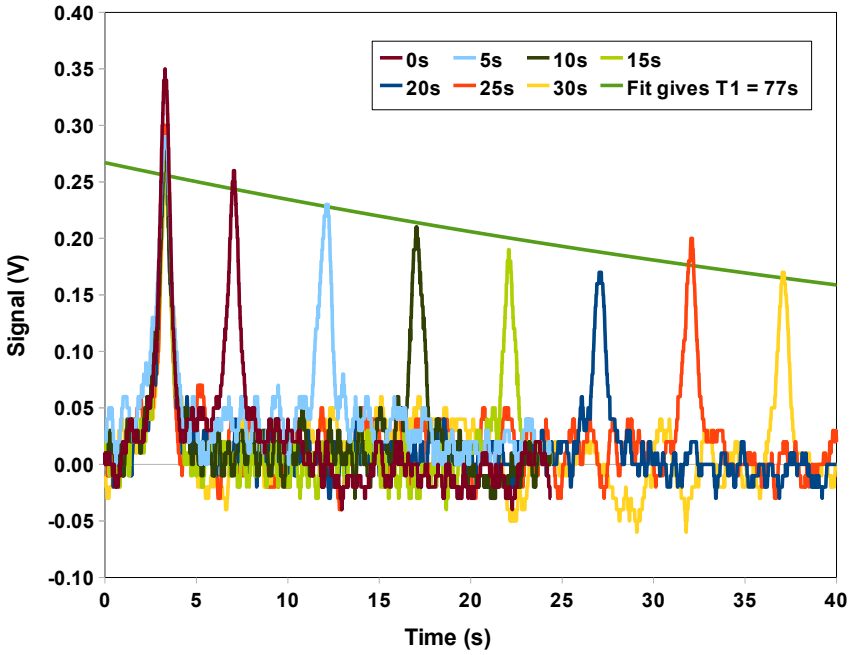

Figure 4.11: Experimental data to determine the T_1 relaxation time. The time between the peaks was increased to allow more Xe-129 to relax before the second pass through resonance. This leads to a exponential drop in the second peak magnitude. The second peak was normalized using the first peak magnitude as described in the text. The T_1 relaxation time is extracted by an exponential fit over the second peaks.

Figure 4.11 displays the oscilloscope traces acquired by conducting this procedure for waiting times varying from zero to 30 seconds. Note that the time reported in the legend of Fig. 4.11 is the time between the B_0 ramps (region 5 in the schematic presented in Fig. 4.9). Since the ramp sections (region 3 in Fig. 4.9) take a finite time, the actual time between resonance points is actually ~ 4 s longer for these trials.

As stated in the figure caption, the data in Fig. 4.11 has been normalized so that the heights of the first peaks have equal magnitude. This was done using the following procedure. The maximum

signal seen in the peak, in Volts, was taken to be representative of the peak height. A constant vertical scale factor was then applied to the B_1 scan in question, arranged so that the first peak height would be equal to the peak height with the nominal zero second waiting time. No correction offsets was applied; it was assumed that the appropriate offset was zero. Normalizing the data in this way reduced the scatter of the trend seen for the second peak.

The data for the second peak were then fit to an exponential using the following technique. Again the highest signal (now normalized, in Volts) seen in the second peak was taken to be indicative of the peak height. The peak time was taken to be the time at which the highest signal was sensed. The peak heights were assumed to have equal errors of ± 0.02 V over the trials, estimated from the baseline noise observed in Fig. 4.11. The data for times and peak heights were then fit using a least–squares minimization. The data was fit to an exponential function in time. The decay time of the exponential was interpreted as the T_1 relaxation time.

The result of the fit was $T_1 = (77 \pm 24)$ s, and is shown in Fig. 4.12. While this decay time is long by typical NMR standards, it is relatively short for polarized xenon, for which T_1 relaxation times on the length of hours have been observed in the best systems [58]. We now comment on the statistical error in the data due to noise, which we assumed to be equal for the various trials. The noise level in any given point may be estimated from the measured baseline noise away from the peaks in Fig. 4.11. We thereby estimated the error due to noise in our peak measurement to be ~ 0.02 V, from the half-width of the noise. Using this error as a statistical error, fit χ^2 in the least-squares fitting of the exponential gives $\chi^2/\mathrm{dof} = 0.689$. The exponential fit is therefore deemed to be a good representation of the data. A fit to a straight line would also give a good representation of the data, since measurements were only taken for relatively short times. Even a single data point obtained at a greater waiting time t value would have obtained a much better fit, as the time scale investigated is short. This was impossible, mainly for a technical reason. The Techron amplifiers heat up under such a small load (when running in constant current mode) and there was a concern that they could be damaged. A solution to this problem would be to use a superior system more appropriate for the much smaller bandwidth required.

It is believed that our system is limited by a variety of factors, none of which could be studied

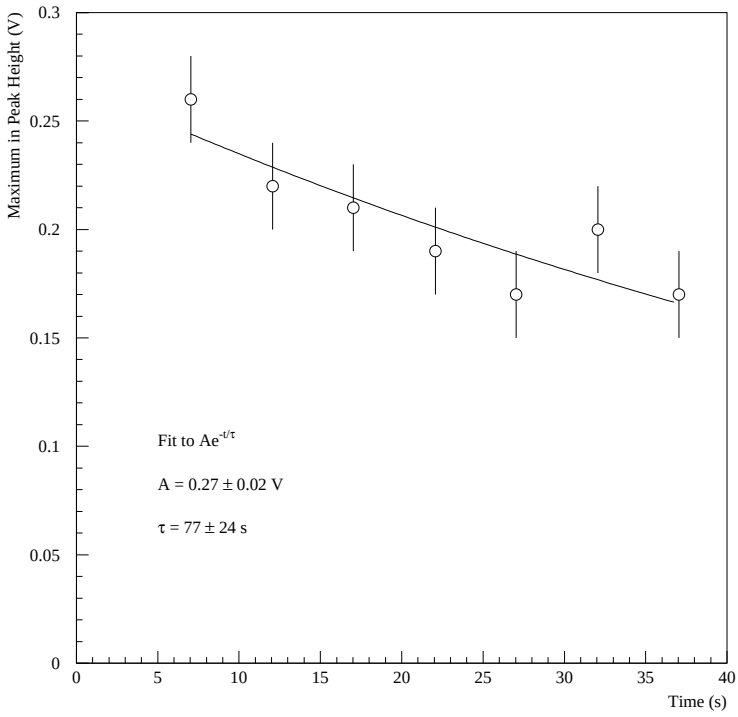

Figure 4.12: Exponential fit used to analyze the T_1 data obtained in Fig. 4.11.

quantitatively in depth for presentation in this thesis. One factor is the leakage of Xe gas out of the measurement volume. If the Xe gas escapes over time, it will result in a loss of signal for longer times. This would manifest itself as a shorter measurement for T_1, in our technique.

A second possibility is diffusion of wrong spin state xenon into the cell from the plastic tubing reaching from the needle valve to the AFP NMR measurement region. Once the first AFP NMR sweep is conducted, the Xe spins in the measurement region are reversed. But wrong spin state Xe atoms can diffuse into the measurement cell over time, displacing correct spin state Xe atoms and diluting the Xe polarization in the measurement region. This effect would manifest itself as a decrease to an equilibrium polarization after a sufficient time that the two spin populations could fully mix. The volume of the AFP NMR measurement region may be approximated as the volume of the plastic bottle used, in this case 147 mL. The volume of the region of tubing from the needle valve to the bottle is 21.8 mL. Based on the ratio of volumes, we therefore expect the signal to relax to a value of 87% of the original value after full mixing of the two spin states has been reached. For

the data presented in Fig. 4.11, this ratio has been reached. It therefore is possible that diffusion mixing of this sort has saturated to volume on the time period of these measurements.

A third possible explanation for the poor T_1 time is surface quality. The plastic bottle used for the AFP NMR measurement volume was borrowed from an Earth's field NMR/MRI experiment done in the Advanced Physics Laboratory at the University of Winnipeg. It was not been cleaned or prepared using any special surface treatment techniques. Cells typically would be cleaned and coated more carefully with polarization preserving materials (e.g. SurfaSil), if the goal was to increase the relaxation time. The other surfaces in the polarizer were treated more carefully. Furthermore, a non-magnetic (but still metallic) needle valve was used, based on the experience of the NRC-SIMS group.

A fourth and final possible explanation for the short T_1 time is poor magnetic field homogeneity. This typically manifests itself as a short T_2^* time. For the neutron EDM experiment, it is primarily this sort of relaxation that we are most interested in.

Finally, we note another interesting feature of Fig. 4.11, which is that the difference in heights between the first peak and second peak in any given oscilloscope trace is significantly larger than the drop in height of the second peak over the various trials. This can be explained by a poor AFP spin reversal efficiency, likely resulting from a poor transverse relaxation time T_2 (also possibly arising from xenon diffusion from the transport tube into the experimental volume as mentioned previously). During the resonances in Fig. 4.11, the Xe spins are fully in the transverse (xy) plane and may experience T_2 relaxation.

Figure 4.13 shows the data obtained from using multiple AFP spin flips to acquire T_1 data. A second sequence, indicated by the blue line in Fig. 4.13, is similar to the one in Fig. 4.6 but with the AFP ramp (indicated by region 3 in Fig. 4.6) repeated three times. This method was initially used as it would give multiple resonance passes at different times, resulting in a simple sequence for obtaining the T_1 relaxation time. It is clear, however, that this method results in a very short relaxation time, as the entire signal is washed out after just $\sim$ 25 s. It is believed that this loss in signal is primarily due to transverse relaxation occurring during the resonance points, and this resulted in us using a different sequence (the one shown in Fig. 4.9 and previously

discussed) to acquire T_1 relaxation time data. For polarized noble gases, T_2 can be more strongly

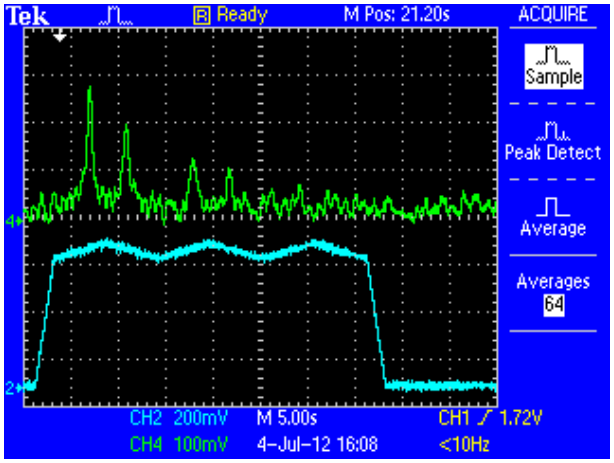

Figure 4.13: Data obtained for determining the T_1 relaxation time using an alternate AFP sequence. The sequence is multiple loops over the two AFP ramps (B_0 field current monitor is shown in blue), producing multiple resonance passes at varying times (signal shown in green). Ultimately, this ramp sequence was not used, for reasons discussed in the text.

affected by magnetic field inhomogeneities than T_1. The inhomogeneities result in dephasing as the spins rapidly precess in the transverse plane. The transverse spin relaxation time T_2 is also still expected to be quite long for polarized noble gases, because the dephasing may be countered by diffusion, so that spins can sample the average B_0 field. In general, a careful study of the various timescales involved is required to disentangle the effects. For now we suggest that this could be another manifestation of poor magnetic field inhomogeneity.

The T_2 relaxation was studied further, though unsuccessfully, using a different NMR technique. This is described in the next Section (Section 4.3.5).

Although some of the four mechanisms affecting the extracted T_1 relaxation time could in principle be studied using the existing apparatus, it was deemed more worthwhile to begin fixing the obvious deficiencies. This is discussed further in Chapter 5. The results presented in this thesis therefore represent the first system produced. Significant improvements to the system are planned.

4.3.5 T_2 Measurement

We attempted to measure T_2 using the NMR technique of free induction decay (FID). The B_0 magnetic field was set to a constant value at the central resonance value found experimentally using

the AFP-NMR sweep sequence. A $\frac{\pi}{2}$-pulse was applied by turning the B_1 field on for a time t (as discussed in Section 3.1.4), flipping the spins into the xy-plane. We then selected $B_1 t$ such that the RF pulse produced a wide NMR linewidth, so that the signal from FID would be easier to detect. Once the B_1 field was switched off, a time varying signal at the Larmor frequency was searched for. This was done using a few different techniques. One technique is to simply examine the oscilloscope trace for the pick-up coil input directly to the oscilloscope. This was confounded by noise and was unsuccessful. A second technique was attempted using the lock-in amplifier. Unfortunately, since the B_1 signal is used as a reference, this technique would be expected to produce a beat signal being detected by the lock-in amplifier at $\omega - \omega_0$ as the Xe atom signal comes in and out of phase with the B_1 reference signal (which persists despite the B_1 driving field being switched off).

A technical detail is that during these tests, significant cross-talk between the B_1 coil and the pick-up coil was experienced. When using the lock-in technique, a trade-off between the lock-in time constant and the noise had to be made. But, because of the large cross-talk, longer time constants would cause the cross-talk to persist longer, into the measurement region. What results in the lock-in signal is therefore a mixture of cross-talk, signal and noise - confounded by the lock-in time constant setting.

Ultimately, a clear FID signal was never found. To achieve a clear signal, several improvements are likely needed: increased magnetic field homogeneity to increase T_2^* and giving more time to observe the signal, more purely orthogonal coils resulting in less crosstalk, and increased polarization resulting in a larger signal. The measurement is fraught with all the same issues as our T_1 extraction technique, and is in addition particularly more sensitive to magnetic field inhomogeneity. As mentioned in Section 4.3.4, this leads to fast dephasing times and a very small value of the effective transverse relaxation time T_2^* (also discussed in Section 3.1.6). The measurement is not inconsistent with the observation of the smaller first to second peak height from Section 4.3.4. Based on those measurements, the T_2 time must be at least the resonance width, or else the second peak would not be observed. This implies $T_2 \gtrsim 1$ s.

A hybrid technique could also be tried, where the ramp (indicated by region 3 in Fig. 4.9) is continually lengthened until the second peak becomes small. The field could then be shimmed until

very slow ramp rates can be achieved. This would give a higher likelihood of success for FID mode. Or a mode more akin to Rabi flopping (with B_1 on continually) could be tried.

The next iteration of the AFP-NMR setup will have new a B_0 coil with better field homogeneity, and higher B_0 capability as discussed in Chapter 5.

4.4 Calculating Xenon Polarization

The net polarization of the xenon is calculated by comparing the signal strength given by the xenon to the signal strength of a similar sample of known polarization [53, 54]. Water is used as a calibration source since the Boltzmann polarization is known for protons placed in a known magnetic field. The majority of experimental factors are held constant so that the signals can be accurately compared. The main experimental difference is that the resonant frequency is considerably smaller for Xe if using the same B_0 field, as we did. This lower operating frequency results in a lower gain from the inductive pick-up and needs to be accounted for.

In general, there are four factors relating the xenon polarization to the known Boltzmann polarization of water: signal strength difference, difference in magnetic moment, number of active spins in the sample and electronic gain factors [41]. This results in the following equation for the calibrated xenon polarization P_{Xe}:

$$P_{\mathrm{Xe}} = P_{\mathrm{p}} \frac{S_{\mathrm{Xe}}}{S_{\mathrm{p}}} \left| \frac{\mu_{\mathrm{p}}}{\mu_{\mathrm{Xe}}} \right| \frac{N_{\mathrm{p}}}{N_{\mathrm{Xe}}} \frac{G_{\mathrm{p}}}{G_{\mathrm{Xe}}}, \tag{4.2}$$

where P represents polarization, S represents signal strength, μ represents the magnetic moment, N represents the number of spins, and G represents an overall gain factor that includes the effects due to the quality factor Q of the tuned pick-up coil and the resonant frequency difference. The subscript attached to each signal refers to the fact that, in general, the quantity will depend on the nucleus in question (Xe for xenon and p for proton).

Proton Thermal Polarization

The proton thermal polarization arises due to a small difference in energy between the spin up state and the spin down state in the presence of a uniform magnetic field. This is represented symbolically in the following equation:

$$P_p = \frac{N_\uparrow - N_\downarrow}{N_\uparrow + N_\downarrow}. \tag{4.3}$$

Here $N_\uparrow$ is the number of protons in the spin up state and $N_\downarrow$ is the number of protons in the spin down state. The spin up state can be considered aligned with the magnetic field and is the lower energy state. At finite temperature T, more protons, will be in the lower energy state leading to a small net polarization. This can be calculated from the Boltzmann distribution. The fraction of protons in the up state is

$$\frac{N_\uparrow}{N_{\text{Total}}} = \frac{e^{-E_\uparrow/kT}}{e^{-E_\uparrow/kT} + e^{-E_\downarrow/kT}},$$

whereas the fraction in the down state is

$$\frac{N_\downarrow}{N_{\text{Total}}} = \frac{e^{-E_\downarrow/kT}}{e^{-E_\uparrow/kT} + e^{-E_\downarrow/kT}}.$$

Here $E_\uparrow = -\left|\mu B_0\right|$ and $E_\downarrow = +\left|\mu B_0\right|$ are the energies of the spin up and down states, respectively, and k is Boltzmann's constant.

These results can be substituted into Equation 4.3 to give

$$P_p = \frac{e^{-E_\uparrow/kT} - e^{-E_\downarrow/kT}}{e^{-E_\uparrow/kT} + e^{-E_\downarrow/kT}} = \tanh\frac{\left|\mu B_0\right|}{kT} = \tanh\frac{\hbar\omega_0}{2kT}. \tag{4.4}$$

At room temperature (298 K), the proton polarization is extremely small. For the magnetic field used here, the Larmor frequency is $\omega_0/2\pi = 25.8$ kHz and $P_p = 2.0775 \times 10^{-9}$.

Calculating the Number of Active Nuclei N

The xenon and water entered identical equal volume plastic bottles centred in the AFP setup. The water bottle was capped and filled with de-ionized water. The number of spins (protons) present in the bottle of water is

$$N_p = V_{\mathrm{H_2O}} \cdot \rho_{\mathrm{H_2O}} \cdot \frac{1}{m_{\mathrm{H_2O}}} \cdot N_{\mathrm{A}} \times 2 \tag{4.5}$$

where $V_{\mathrm{H_2O}}$ is the water volume, $\rho_{\mathrm{H_2O}}$ its density, $m_{\mathrm{H_2O}}$ its molar mass, and N_{A} is Avogadro's number. The factor of two arises because each water molecule has two protons. For our bottle of water $V_{\mathrm{H_2O}} = 147$ mL and therefore, $N_p = 9.83 \times 10^{24}$.

For xenon NMR, a small hole was made in the cap of the bottle to allow the gas to flow through. The gas composition was assumed to be unchanged from the initial conditions. Thus, treating the mixture as an ideal gas at atmospheric pressure and room temperature, the number of Xe-129 nuclei in the sample can be calculated as follows:

$$N_{\mathrm{Xe}} = V_{\mathrm{Xe}} \cdot \frac{1}{V_{\mathrm{Ideal}}} \cdot N_{\mathrm{A}} \times 0.264 \times 1.00\% \tag{4.6}$$

where V_{Xe} is the volume of the bottle (147 mL), $V_{\mathrm{Ideal}} = 22.465$L/mol is the molar volume of an ideal gas at 298K and 101.325 kPa, 0.264 is the isotopic abundance of Xe-129 and 1.00% is the concentration of Xe in the gas mixture, as specified by the manufacturer. As a result our bottle will contain $N_{\mathrm{Xe}} = 1.04 \times 10^{19}$ atoms of Xe-129 once full with gas from the polarizer.

Gain Factor

The gain factor ratio was determined experimentally using a small coil to generate a known dipole field. The coil was fixed on the empty experimental bottle and driven by a function generator, producing a dipole field $m(t) = m \cos \omega t$ inside the pick-up coils. The coil was driven at several differnt currents for each of the two frequencies, 7.2 kHz (xenon) and 25.8 kHz (proton). The current was monitored by measuring the voltage across a 1 Ω resistor in series with the dipole coil to ensure that the same values of m were used at each frequency. The amplitude of the induced voltage in

the pick-up coil was measured using the same electronics as in the AFP experiment described in Section 3.4. The ratio of the magnitudes of the signal measured by the lock-in amplifier at the two frequencies gives the overall gain factor. The results are shown in Table 4.3

Output Voltage (mVpp)	Signal at 7.2 kHz (mV)	Signal at 25.8 kHz (mV)	Gain Factor
200	15.2 ± 0.1	172.2 ± 0.1	11.3
400	30.3	343.3	11.3
600	45.5	515.9	11.3
800	60.6	687.3	11.3
1000	75.8	858.8	11.3

Table 4.3: Data and results for the gain factor determination. Measurements were made for five different output peak-to-peak voltages of the function generator. The current in the dipole was independent of frequency. The overall gain factor is the ratio of the signal at 25.8 kHz divided by the signal at 7.2 kHz. The error in each value recorded in the signal column is 0.1 mV.

A gain factor value of $\left(\frac{G_p}{G_{Xe}}\right) = (11.3 \pm 0.1)$ was found. The value is consistant with expectations. Given that both the induced voltage ($\epsilon = -d\phi/dt$) in the coil and its quality factor ($Q = \omega_0 L/R$) scale as ω, one expects that the gain factor to be the square of the ratio of frequencies or $(25.8/7.2)^2 = 12.84$. This assumes that the resistance R of the coil is independent of frequency, which in general it is not. If, on the other hand, one assumes that R is limited at both frequencies by the electromagnetic skin depth ($\delta = \sqrt{2/\sigma\omega\mu}$, where σ is the electrical conductivity and μ is the magnetic permeability of the copper wire) then the gain factor should be $(25.8/7.2)^{1.5} = 6.78$. Our value is much closer to the former and is consistant with the fact that the decrease in skin depth for copper over our frequency range (0.9 mm at 7.2 kHz compared to 0.5 mm at 25.8 kHz) should not greatly reduce the effective cross-sectional area of the 30 gauge wire (0.26 mm diameter) used in the pick-up coil [50].

The calculated gain factor is 12% smaller than the expected gain factor of 12.84, not accounting for any effect of the resistance. This could be accounted for by improper tuning of the resonance circuit. If the actual resonance frequency is slightly off from the measured frequency, a signal will still appear, due to the width of the observed signal. Considering that both experimental frequencies may be off from the actual resonance frequency could account for the 12% loss in gain between the two frequencies.

Error in Signal Strength

The AFP signal strength of both water and xenon experienced a day to day variation of 10%. The source of this uncontrolled systematic error was never located. It is expected to be related to local field fluctuations and small motions of the apparatus.

For xenon specifically, the signal difference could be due to the number of nuclei present in the bottle changing since this number was in a state of constant change due to the flow through nature of the setup and the possibility of xenon leaking out of the bottle. Furthermore, the polarization calculation assumes that the pressure in the AFP region is at 101.325 kPa all the time, and does not account for daily fluctuations. This error would not be present in the water sample. These sources of error were therefore combined and treated by measuring the reproducibility of signal strengths over multiple trials, for which we feel the 10% figure is adequate to encompass the random error.

A first test when using the xenon polarizer was to check the AFP setup by running a sample with water. Similarly, a xenon trial was always completed at the start of testing as a baseline for the xenon polarizer. This trial allowed a check that the polarizer was heated and functioning properly. Experience was gained on signal strength over several months, allowing for measurements of day to day fluctuations to be quantified. Based on this experience the monthly average signal on the oscilloscope for water was (200 ± 50) mV and for xenon was (300 ± 50) mV. These measurements were taken using the experimental parameters listed in Appendix B.

A systematic error during adiabatic spin transport was unaccounted for. All AFP NMR measurements were taken in the experimental volume after the SEOP cell, several meters away. The hyperpolarized xenon had to travel through nearly 3 m of tubing before reaching the experimental volume and some polarization is lost during transport. This error can be eliminated by performing AFP NMR directly in the SEOP cell. Another option could be to freeze the hyperpolarized Xe into a solid which is then transported and reheated for AFP NMR experiments.

Xe Polarization

In Table 4.4, we gather the relevant factors for the determination of the Xe polarization. Using Equation 4.2, we thereby obtain the polarization $P_{\mathrm{Xe}} = (12 \pm 4)\%$. The error is dominated by the typically daily reproducibility of the signal size observed in the water AFP NMR signal, which is a slightly smaller signal than that from Xe-129.

Parameter	Water	Xe-129
Signal Strength	(200 ± 50) mV	(300 ± 50) mV
μ	2.7928 μ_{n}	-0.7768 μ_{n}
N	9.83×10^{24} spins	1.04×10^{19} spins
G	(11.3 ± 0.1)	1 (normalized)

Table 4.4: Parameters for calculating Xe-129 polarization. μ_N is the nuclear magneton constant. Any error in N is combined into the error in signal strength, as discussed in the text.

The polarizer at NRC-SIMS achieved typical polarizations of $5 - 6\%$ [52]. Our polarizer represents a significant improvement in Xe-129 polarization compared to the original setup at NRC-SIMS. The largest contribution to this improvement is likely the new 75 W diode laser, whereas NRC-SIMS relied on only 30 W of laser power from a broader diode than D1, even pressure broadened. Although we typically used the laser at 60 W, this still represents a 100% increase in laser power, and could explain most of the increase in polarized xenon obtained from the polarizer at the University of Winnipeg. For a neutron EDM experiment the polarization level needs to be improved, as we desire low quantities of highly polarized Xe-129, with polarization in excess of 50%.

High xenon polarization, in excess of 50%, is possible using superior cell designs and higher powered lasers [55, 56, 57]. For example, in Ref. [55], the experimental region consists of multiple rubidium reservoirs (called the Rb saturator) arranged in a spiral around a central SEOP cylinder. The Xe mixture enters the Rb saturator and flows past as the rubidium is vaporized. This mixture of Rb and Xe enters the central cylinder, where SEOP takes place. The entire setup is arranged in a vertical column, 1.8 m in length, with the laser light incident from the top. The Rb cools as it travels up the cylinder, condensing out before the xenon exits the cylinder at the top. After the SEOP cell, the Xe is analyzed and collected in a freezeout spiral. This type of a cell reports a Xe-129 polarization of 64% at a flow rate of 0.31 litres/hour using a laser power of ~ 90 W. A cell

of this type could be necessary for obtaining the desired polarization of Xe-129 for use in a neutron EDM experiment.

Chapter 5

Conclusions and Future Work

5.1 Conclusion

A new Xe polarizer at the University of Winnipeg was assembled and tested. The polarizer was used to deliver polarized Xe to a measurement cell located in a low field AFP NMR spectrometer. The new feature of the polarizer is a higher power diode laser. The AFP NMR spectrometer was used to perform initial measurements characterizing the polarizer's performance. The Xe-129 polarization was determined to be $P_{\mathrm{Xe}} = (12 \pm 4)\%$, calibrated to a Boltzmann polarized water sample. The error was dominated by day-to-day fluctuations on the AFP signal size of both Xe and water. The AFP NMR system produced a few key results demonstrating its own performance. In particular, a signal decay time of (77 ± 24) s was observed for the disappearance of signal in the longitudinally polarized Xe, where the stated uncertainty is only statistical. This was interpreted as a T_1 measurement. Systematic uncertainties due to diffusion of the two spin populations of the gas, magnetic field inhomogeneity and surface quality were suggested as possible reasons for the low T_1 value compared with other experiments. The transverse relaxation time T_2 was suggested to be larger than ~ 1 s by the AFP NMR measurements, but a signal using FID could not be detected and no more quantitative determination could be made.

5.2 Future Work

Upgrades are planned to both the polarizer and the experimental setup. A fully computerized setup is planned for the polarizer, with digital control and monitoring of pressures, flow rates and temperatures. The SEOP cell itself can be upgraded to increase the length of the cell. This will allow for more photon interaction between the rubidium and the circularly polarized laser light along with a longer interaction time for spin exchange, resulting in an expected increase in polarization.

A new SEOP cell could be created, possibly similar to the cell in Ref. [55]. This would help increase the polarization of the hyperpolarized Xe-129 to the level required for use in a neutron EDM experiment. Freezing the hyperpolarized xenon could also be investigated as a way to transport the hyperpolarized gas to the experiment. This can be used as only small quantities of hyperpolarized Xe-129 are needed, and only a small amount of polarization is lost during the freezing process. The neutron EDM experiment requires the T_1 and T_2 times to be as long as possible. Ref. [58] states that the relaxation rate of pure xenon gas is limited by wall induced relaxations, and reports T_1 times of $6 < T_1 < 10$ hours and T_2^* times of $4 < T_2^* < 6$ hours in the nearly ideal magnetic conditions (gradients of order pT/cm) within the "magnetically best shielded room on Earth". The glass used to construct the cell is aluminosilicate glass, with no mention of any coating used.

Thus, a long T_1 time requires a well constructed experimental cell, typically with a siloxane surface coating to reduce surface induced relaxations [37]. This however, is not a property of the polarizer but rather a property of the experimental cell that the hyperpolarized xenon is used in. A long T_2 could be obtained in a similar fashion. An improved transport system to the experimental volume in conjunction with better magnetic field homogenity and suppressed wall relaxations from the experimental cell should produce much longer transverse relaxation times T_2, with the major factor being field homogenity influencing T_2^*.

New B_0 coils have been designed and are currently under construction for the AFP-NMR setup. The new coil setup will consist of a set of 5 coils precision mounted and wound for improved homogeneity. The new coils will also be better suited for the power supply that is currently being used, allowing for higher magnetic fields to be reached if necessary. This is expected to greatly

improve both T_1 and T_2 lifetimes.

Appendix A

Operation of the U of W Xenon Polarizer

Directions for use of the University of Winnipeg Xenon Polarizer and AFP setup. Parameters for equipment that needs to be turned on and set can be found in Appendix B and Section 3.4. These directions assume that everything is already connected and ready to use.

A.1 Turning on the Xenon Polarizer

1. Ensure all doors are closed and laser safety signs are on the exterior of the doors.
2. Turn on laser chiller plate cooling system.
3. Turn on power supply for the solenoid. This will begin to heat the area around the SEOP cell.
4. Open gas flow valve on the main tank. Check regulator and that the line pressure is ok.
5. Purge gas lines up to the entrance of the SEOP cell, in order, opening valves as the previous lines are purged. A purge should be done in three places. a) before pressure gauge, b) in between the moisture and oxygen traps and c) before the SEOP cell.
6. Ensure that all lens caps are removed from optics.
7. Turn on spectrometer and remove lens cap from spectrometer fiber housing.

8. Turn on thermometer.

9. Put on laser safety goggles.

10. Turn the key on the laser current control box. Laser should not be on at this point. Ensure nothing unwanted is in the beam path, and a proper beam dump is in place.

11. Turn laser on and set to desired current.

12. Turn on heater tape for rubidium oven.

13. Open gas flow valves to SEOP cell. Needle valve should still be closed.

14. Wait. About 20 minutes, but will depend on the cell being used. This is a good time to turn on the AFP system.

15. Polarizer should be working when the oven temperature reaches $\approx 200\,^{\circ}\mathrm{C}$ and the cell temperature is $60 - 70\,^{\circ}\mathrm{C}$

16. Open needle valve to desired flow rate.

17. Check for signal using AFP NMR setup.

A.2 Turning on the AFP NMR Setup

1. Ensure Techron amplifier has a load attached.

2. Turn on Techron amplifier, oscilloscope, lock-in amplifier (with attached pre-amp), Techmag boxes, computer and signal generator. All equipment parameters should still be set (from last turn on). If not, use the parameters listed in Appendix B.

3. Open NTNMR software on the computer and locate AFP ramp file. Open the amplifier sequence.

4. Ensure the correct capacitance tuning box is attached for the frequency desired.

5. Zero the signal on the lock-in amplifier using the compensation coil signal, channel 2 on the signal generator. This can be done by recording the signal (on the lock-in) given when the compensation coil is off. This may require changing the window size on the lock-in amplifier. Turn off the B_1 coil and match the recorded signal in the compensation coil, but 180° out of phase. Turn on both the B_1 and compensation coil and set the amplifier window back to experimental level. Fine tune any additional adjustments by changing the amplitude and phase of the compensation coil until the signal is close to zero. Once the signal is close, the offset command on the lock-in amplifier can be used to zero the signal.

6. Enable the Techron amplifier.

7. Re-zero the lock-in by pressing the offset button on both channels.

8. AFP NMR setup is now ready.

A.3 Turning Off Xenon Polarizer

1. Turn off heater tape.

2. Isolate the SEOP cell by closing needle valve and cell valves in reverse order of gas flow.

3. Turn off solenoid and spectrometer.

4. Close remaining gas valves in reverse gas flow order finishing with the main valve on the gas canister. Be aware of the secondary laser beam.

5. Wait a few (5) minutes as the rubidium oven cools, the laser should remain on. This stops rubidium from building up on the optical face of the cell.

6. Turn off the laser and chiller plate. Laser should be ramped down to 0A, then output turned off, then the key turned. This prevents a unexpected high power beam when the output is turned on.

7. Replace lens caps onto optics.

8. If desired, flood gas flow system with argon to help preserve the SEOP cell.

A.4 Turning Off AFP NMR Setup

1. Disable Techron amplifier.

2. Turn off all electronics.

Appendix B

Experimental Parameters

Experimental parameters that were used to run the polarizer and AFP-NMR setup are summarized here.

B.1 Polarizer

- **Regulator valve on main gas supply tank:** 50 PSI
- **Flow rate (set by needle valve):** 0.2-0.25 slm
- **Temperature of Rb oven (controlled by autotransformer set at 30%):** $\approx 200°C$
- **Temperature of SEOP cell:** $(60 - 80)°C$
- **Laser chiller plate temperature:** $22°C$
- **Laser current:** 25 A
- **Laser base temperature (for reference):** $(24.9 - 25.0)°C$
- **Solenoid current:** 3 A
- **Quarter wave plate angle:** $80°$
- **Spectrum peak centre:** 794.95 nm

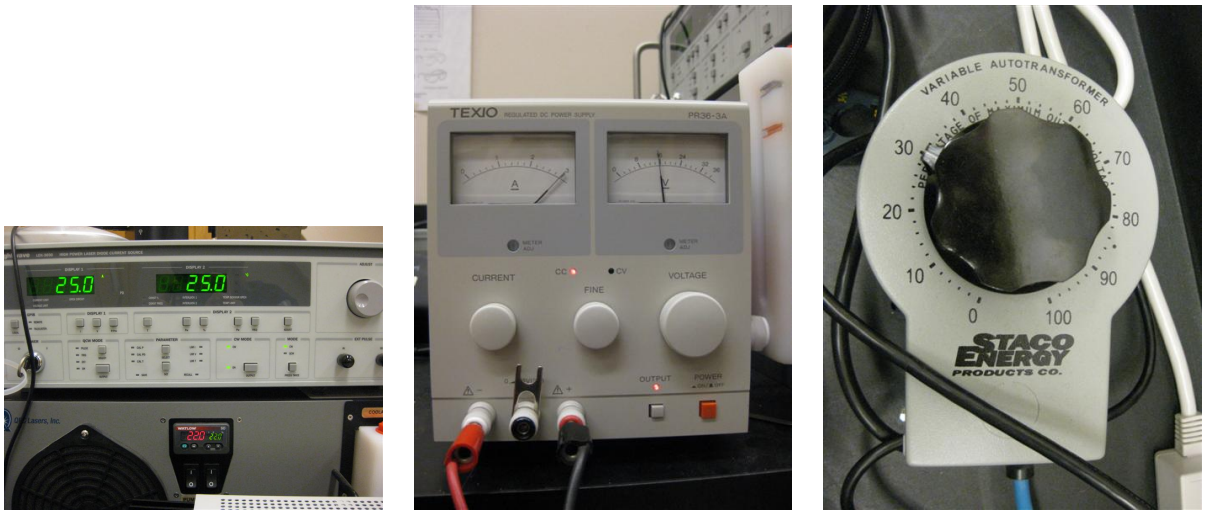

(A) (B) (C)

Figure B.1: Experimental parameters of polarizer equipment. (A) Laser current supply and chiller plate settings. (B) Solenoid power supply settings. (C) Variac setting.

B.2 AFP-NMR electronics

- **Preamplifier:** A-B setting
- **Lock-in Amplifier:** Time constant: $100ms$, $12dB$. Sensitivity: $500\mu V$. Signal: A-B, DC, Float. Reserve: *normal*.
- **Function generator (Channel One):** Frequency: depends on nuclei, Amplitude: 1.4Vrms, Offset: 0V, Phase: 0°.
- **Function generator (Channel Two):** Frequency: depends on nuclei, Amplitude: Varies, Offset: 0V, Phase: Varies.
- **Oscilloscope:** Ch 1: Trigger, Ch 2: current monitor, Ch 3: x signal from lock-in. Ch 4: y signal from lock-in. X scale: Varies.

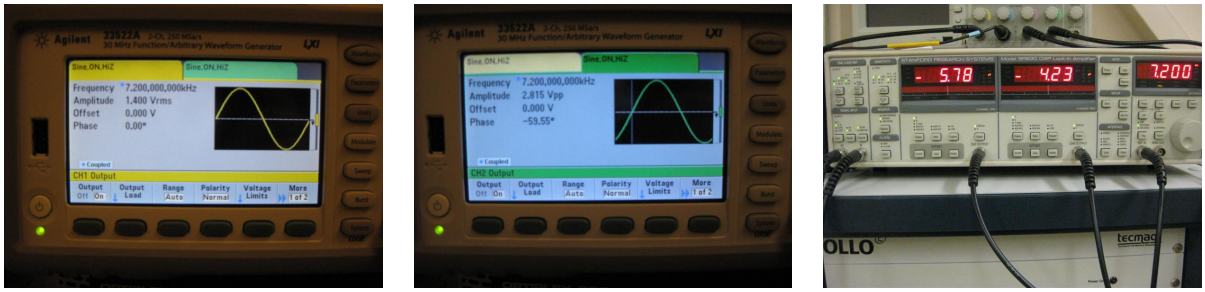

(A) (B) (C)

Figure B.2: Experimental parameters of AFP NMR equipment. (A) B_1 settings. (B) Compensation coil settings. (C) Lock-amp settings.

Bibliography

[1] M. Pospelov, A. Ritz, Ann. Phys **318**, 119 (2005)

[2] J. Engel, M. J. Ramsey-Musolf, U. van Kolck, arXiv:1303.2371v1 [nucl-th] March 10, (2013)

[3] A. D. Sakharov, Sov. Phys. Usp. **34**, 392 (1991). This is a reprint of: A. D. Sakharov, Pis'ma Zh. Eksp. Teor. Fiz. **5**, 32 (1967).

[4] G. R. Farrar, M. E. Shaposhnikov, Phys. Rev. Lett. **70**, 2833 (1993)

[5] D.E. Morrissey *Fundamental Symmetries and Cosmology*, TRIUMF Summer Institute, August 6, (2012)

[6] D.E. Morrissey, M. J. Ramsey-Musolf, New Journal of Physics **14** (2012) 125003

[7] S. J. Huber, M. Pospelov, A. Ritz, Phys Rev D **75**, 036006 (2007)

[8] C. A. Baker *et al.*, Phys. Rev. Lett. **97**, 131801 (2006)

[9] N. Ramsey, Phys. Rev. **100**, 1191 (1955)

[10] N. Ramsey, Rep. Prog. Phys. **45**, 95 (1982)

[11] N. Ramsey, *Experiments with separated Oscillatory Fields and Hydrogen Masers*, Nobel Lecture, Dec. 8 (1989)

[12] N. Ramsey, Phys. Rev. **78**, 695 (1950)

[13] J. M. Pendlebury *et al.*, Phys. Rev. A **70**, 032102 (2004)

[14] S. K. Lamoreaux, R. Golub, Phys. Rev. A **71**, 032104 (2005)

[15] K. F. Stupic *et al.*, J. Mag. Res. **208**, 58 (2011)

[16] M. Berry, Proc. R. Soc. London, Ser. A **392**, 45 (1984)

[17] D. J. Griffiths, *Introduction to Quantum Mechanics - 2nd edition*, Pearson Education **2005**

[18] F. Bloch, A. Siegert, Phys. Rev. **57**, pg. 522 (1940)

[19] Y. Masuda, *et al.*, Phys. Lett. A. **376**, 1347 (2012)

[20] M. J. Schonhuber, IEEE Transactions on Power Apparatus and Systems **PAS-88**, 100 (1969)

[21] A. Miller, presentation at the Canadian UCN Collaboration Meeting, University of Manitoba and University of Winnipeg, Winnipeg, Canada, Oct. 3-5 (2012)

[22] J. Martin, *Private Communication*, (2012)

[23] A. Miller, *Private Communication*, (2012)

[24] E. Miller, poster at TRIUMF Summer Institute TSI2012, TRIUMF, Canada, Aug 6-17 (2012)

[25] R. Golub , D. Richardson and S. Lamoreaux, Ultra-Cold Neutrons. IOP Publishing Ltd, **1991**

[26] Y. Masuda, *EDM Review*, presentation at KEK in Tsukuba, Japan, Dec 29-30 (2012)

[27] C. Kittel, *Introduction to Solid State Physics Eighth Edition.* John Wiley and Sons, Inc. **2005**

[28] B. C. Grover, Phys. Rev. Lett. **40**, 391 (1978)

[29] T. G. Walker, W. Happer, Rev. Mod. Phys., **69**, 629 (1997)

[30] S. Appelt, *et al.*, Phys Rev. A. **58**, 1412 (1998)

[31] R. L. deZafra, Am. J. Phys. **28**, 646 (1960)

[32] R. Benumof, Am. J. Phys. **33**, 151 (1965)

[33] W. Happer, Rev. Mod. Phys., **44**, 169 (1972)

[34] Daniel A. Steck, *Rubidium 85 D Line Data*, available online at http://steck.us/alkalidata (revision 2.1.5, 19 September 2012)

[35] F. Calaprice, W. Happer, *et al.* Phys Rev Lett. **54**, 174 (1985)

[36] W. Happer, *et al.*, Phys. Rev. A. **29**, 3092 (1984)

[37] S. Breeze, S. Lang, *et al.* J. Appl. Phys. **87**, 8013 (2000)

[38] I. Moudrakovski, *et al.*, Chem. Materials **12**, 1181 (2000)

[39] B. Driehuys, G. D. Cates, E. Miron, K. Sauer, D. K. Walter, W. Happer, Appl. Phys. Lett.**69**, 1668 (1996)

[40] K. Knagge, J. Prange, D. Raftery, Chem. Phys. Lett. **397** 11 (2004)

[41] S. E. Korchak, W. Kilian, L. Mitschang, Appl. Magn. Reson. **44**, 65 (2013)

[42] H. Dong *et al* Supercond. Sci. Technol. **21** 115009 (2008)

[43] *Fundamental Physical Constants* http://physics.nist.gov

[44] H. Anderson, Phys. Rev., **76**, 1460 (1949)

[45] I. I. Rabi, N. F. Ramsey, J. Schwinger, Rev. Mod. Phys. **26**, 167 (1954)

[46] H. G. Hecht, *Magnetic Resonance Spectroscopy*, John Wiley and Sons, Inc. **1967**

[47] F. Bloch, Phys. Rev **70**, 460 (1946)

[48] A. Abragam, *Principles of Nuclear Magnetism*. Oxford University Press **1961**

[49] C. P. Bidinosti, I. S. Kravchuk, M. E. Hayden, Journal of Magnetic Resonance **177** 31 (2005)

[50] J. Wiebe, *Design and construction of custom inductive receive coils for low-feld AFP NMR using hyperpolarized xenon*. Unpublished undergraduate thesis, **2011**

[51] T. Hertsens, ILX Lighwave Application Note 5 available online as *Overview of Laser Diode Characteristics* at http://www.newport.com/Application-Notes-Technical-Notes-and-White-Papers/1014852/1033/content.aspx.

[52] I. L. Moudrakovski, *et al.*, Journal of Magnetic Resonance **144**, 372 (2000)

[53] T. Pavlin, Ph.D. Thesis, California Institute of Technology, (2003)

[54] M. Romalis, Ph.D. Thesis, Princeton University, (1997)

[55] I. C. Ruset, S. Ketel, F. W. Hersman, Phys. Rev. Lett **96**, 053002 (2006)

[56] U. Ruth, *et al*, Appl. Phys. B **68**, 93 (1999)

[57] A. L. Zook, B. B. Adhyaru, C. R. Bowers, Journal of Magnetic Resonance **159**, 175 (2002)

[58] M. Burghoff, *et al.*, Journal of Physics: Conference Series **295**, 012017 (2011)

[59] A. Oros, N. Jon Shah, Phys. Med. Biol. **49**, R105 (2004)